J. Fluid Mech. (2022), *vol*. 950, A21, doi:10.1017/jfm.2022.742

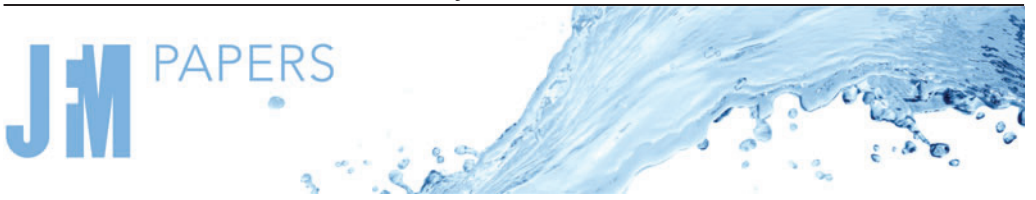

Enstrophy production and flow topology in compressible isotropic turbulence with vibrational non-equilibrium

Qinmin Zheng[1,2], Yan Yang[1,2], Jianchun Wang[1,2,†] and Shiyi Chen[1,2,3]

[1]Department of Mechanics and Aerospace Engineering, Guangdong-HongKong-Macao Joint Laboratory for Data-Driven Fluid Mechanics and Engineering Applications, Southern University of Science and Technology, Shenzhen 518055, PR China

[2]Southern Marine Science and Engineering Guangdong Laboratory (Guangzhou), Guangzhou 511458, PR China

[3]State Key Laboratory of Turbulence and Complex Systems, Peking University, Beijing 100871, PR China

(Received 15 January 2022; revised 28 June 2022; accepted 19 August 2022)

Enstrophy production and flow topology are numerically investigated for statistically stationary compressible isotropic turbulence in vibrational non-equilibrium with a large-scale thermal forcing. The net enstrophy production term is decomposed into solenoidal, dilatational and isotropic dilatational terms based on the Helmholtz decomposition. From the full flow field perspective, the net enstrophy production mainly stems from the solenoidal term. For the dilatational and isotropic dilatational terms, although their local magnitudes can be considerable, the positive values in the compression region and the negative values in the expansion region cancel out on average. For the solenoidal component of the deviatoric strain-rate tensor, the statistical properties of its eigenvalues and alignments between vorticity and its eigenvectors are nearly independent of the local dilatation and vibrational relaxation. The solenoidal components of enstrophy production along three eigendirections are thus mainly affected by the vorticity. For the dilatational component of deviatoric strain-rate tensor, the statistical properties of its eigenvalues and alignments between vorticity and its eigenvectors closely relate to the local dilatation and vibrational relaxation. The dilatational components of enstrophy production along three eigendirections are therefore affected by the vorticity, eigenvalues and alignments between the vorticity and eigenvectors. The topological classification proposed by Chong *et al.* (*Phys. Fluids*, vol. 2, issue 5, 1990, pp. 765–777) is employed to decompose the flow field into various flow topologies. In the strong compression and strong expansion regions, the relaxation effects on the volume fractions

† Email address for correspondence: wangjc@sustech.edu.cn

of flow topologies and their relative contributions to the local enstrophy production are significant.

Key words: compressible turbulence, isotropic turbulence

1. Introduction

The small-scale dynamics of turbulence can be described using the velocity gradient tensor, and is closely related to many important turbulent flow processes, including viscous dissipation of kinetic energy, enstrophy production and intermittency. There are numerous investigations on the statistical properties of the vorticity field, enstrophy transfer and strain-rate tensor for incompressible turbulent flows (Hamlington, Schumacher & Dahm 2008; Wallace 2009; Zhou *et al.* 2016; Carter & Coletti 2018). Ashurst *et al.* (1987) pioneered numerical investigations of the alignments between vorticity and eigenvectors of the strain-rate tensor in incompressible isotropic turbulence and homogeneous shear turbulence. They found that the vorticity tends to align with the intermediate strain-rate eigenvector, and the strain-rate eigenvalues have a preferred ratio of $-4.0{:}1.0{:}3.0$ in the highly dissipative region. Tsinober, Kit & Dracos (1992) experimentally investigated the velocity gradients in both homogeneous and inhomogeneous incompressible turbulence based on the multi-hot-wire technique. Their results confirmed the strong tendency of alignment between the vorticity and the intermediate strain-rate eigenvector. Meanwhile, the preferred eigenvalue ratio was found to be $-3.8{:}1.0{:}3.1$, very close to $-4.0{:}1.0{:}3.0$. These behaviours were also observed in the later investigations for a wide variety of incompressible turbulent flows (Lüthi, Tsinober & Kinzelbach 2005; Buaria, Bodenschatz & Pumir 2020). More details about the velocity gradient tensor in incompressible turbulent flows can be found in the comprehensive review by Meneveau (2011).

Compared with incompressible turbulence, there are much fewer investigations on the vorticity field and strain-rate tensor in compressible turbulent flows. Erlebacher & Sarkar (1993) numerically investigated the velocity gradient tensor in a weakly compressible homogeneous shear turbulence. A preferred strain-rate eigenvalue ratio of $-4.0{:}1.0{:}3.0$ and the similar alignments between vorticity and strain-rate eigenvectors were observed as in incompressible flows. Their results revealed that the statistics of the velocity gradient tensor are not significantly modified by the local dilatation when the turbulent Mach number is smaller than 0.3. Furthermore, the most probable eigenvalue ratio for the dilatational component of deviatoric strain-rate tensor is found to be $-2.2{:}1.0{:}1.2$ in the strong compression region, indicating the dominant role of sheet-like structures in this region. Lee, Girimaji & Kerimo (2009) performed numerical simulations of decaying compressible isotropic turbulence with initial turbulent Mach numbers up to 0.885, wherein the strain-rate eigenvalue ratio of $-4.0{:}1.0{:}3.0$ and the alignments between vorticity and strain-rate eigenvectors still hold, although the preferential alignments are weakened in the strong compression region. One can expect that a stronger compression could show observable impacts. For example, in Wang *et al.* (2012), with the turbulent Mach number is around 1.0, although the eigenvalue ratio of the solenoidal strain-rate tensor of approximately $-3.7{:}1.0{:}2.7$ is in good agreement with that in the incompressible turbulence, the eigenvalue ratio of the dilatational strain-rate tensor tends to be $-1.0{:}0.0{:}0.0$ in the high compression region, and the most probable eigenvalue ratio of the strain-rate tensor is approximately $-3.0{:}1.0{:}2.5$ in the overall flow field. They also found that the strong local compression motion enhances the enstrophy production,

while the strong local expansion motion suppresses the enstrophy production by vortex stretching.

A general classification of local flow topology based on the three invariants of the velocity gradient tensor was proposed by Chong, Perry & Cantwell (1990). For incompressible turbulence, the first invariant (P) is null, and the local flow topology is fully characterized by the second (Q) and third (R) invariants. Extensive studies on the statistical properties in the Q–R plane have been performed numerically and experimentally (Nomura & Post 1998; Nomura & Diamessis 2000; Bijlard *et al.* 2010). A universal teardrop shape of the joint probability density function (PDF) between the second and third invariants was observed for a wide variety of incompressible turbulent flows, including wall-bounded flows (Blackburn, Mansour & Cantwell 1996; Chong *et al.* 1998), isotropic turbulence (Ooi *et al.* 1999) and the turbulence/non-turbulence interface in jets (da Silva & Pereira 2008), etc.

Relevant investigations on the flow topology of compressible turbulence are relatively limited (Wang & Lu 2012; Vaghefi & Madnia 2015; Danish, Sinha & Srinivasan 2016; Parashar, Sinha & Srinivasan 2019; Wang *et al.* 2020). Pirozzoli & Grasso (2004) reported that the joint PDFs of the second and third invariants of the velocity gradient tensor in decaying compressible isotropic turbulence share a similar teardrop shape at various initial turbulent Mach numbers. Furthermore, the conditional average of the second invariant of the deviatoric strain-rate tensor with respect to the third one always scales with the 1/3 power of the discriminant of the velocity gradient tensor. Suman & Girimaji (2010) numerically investigated the local flow topology in compressible isotropic turbulence and analysed the dilatational effect on the flow topology. The investigation was based on the joint PDF of the second and third invariants of the velocity gradient tensor conditioned on the local dilatation. They showed that, at low dilatational levels, the local flow topology is similar to incompressible turbulence, while at high dilatational levels, the flow structures are significantly changed. At a higher turbulent Mach number of around 1.0 (Wang *et al.* 2012), in the compression region, the teardrop shape of the joint PDF exhibits a more extended tail in the fourth quadrant, which stems from the shocklet structures. In contrast, in the expansion region, the joint PDF takes a more rounded shape with a shortened bottom-right tail, and a nearly symmetric joint PDF appears in the strong expansion region.

In high-speed flows of practical interest, the hypersonic speed and/or the extreme levels of shear result in a high temperature in the shock layer and boundary layer (Candler 2019). The vibrational non-equilibrium phenomenon resulting from the high temperature thus widely exists in the high-speed flows. The advent of vibrational relaxation has a profound impact on the flow dynamics (Fiévet & Raman 2018; Knisely & Zhong 2020), and renders the statistical properties of compressible turbulence more complicated. The investigations of the statistical properties of compressible isotropic turbulence in vibrational non-equilibrium were pioneered by Donzis & Maqui (2016), and followed by Khurshid & Donzis (2019) and Zheng *et al.* (2020, 2021). In our companion paper (Zheng *et al.* 2021), we numerically simulated the statistically stationary compressible isotropic turbulence in vibrational non-equilibrium with a large-scale thermal forcing. It was revealed that the flow structures and compressibility are significantly modified due to the combined effects of vibrational relaxation and large-scale thermal forcing, especially for the cases with a turbulent Mach number of approximately 0.22. To our knowledge, the statistical properties of the small-scale structures of compressible isotropic turbulence in vibrational non-equilibrium have never been investigated systematically. In this work, we mainly focus on the combined impacts of vibrational relaxation and large-scale thermal forcing on the statistical properties of the strain-rate tensor, vorticity

field, enstrophy production and flow topology. Such a comprehensive investigation would further deepen our understanding of small-scale features of compressible turbulence in vibrational non-equilibrium. The large amount of conditional statistics in current study will contribute to the development of accurate models for compressible turbulence in vibrational non-equilibrium.

The rest of paper is organized as follows. In § 2, the governing equations, thermodynamic and transport properties of compressible turbulence and a brief description of the numerical methodology will be introduced. The one-point statistics of the current simulated flows, including the statistical properties of the strain-rate components and vorticity, are given in § 3. The combined effects of vibrational relaxation and large-scale thermal forcing on the statistical properties of enstrophy production and flow topology are respectively presented in §§ 4 and 5. Finally, a discussion building the connection among various observations and the concluding remarks are provided in §§ 6 and 7.

2. Computational details

2.1. *Governing equations and numerical method*

In the current simulations, non-reactive mono-species gases and Newtonian fluids are considered, for which the dynamic viscosity relies only on the temperature. The dimensionless governing equations for compressible turbulence in vibrational non-equilibrium can be written as follows (Donzis & Maqui 2016; Zheng *et al.* 2021):

$$\frac{\partial \rho}{\partial t} + \frac{\partial (\rho u_j)}{\partial x_j} = 0 \tag{2.1}$$

$$\frac{\partial (\rho u_i)}{\partial t} + \frac{\partial [\rho u_i u_j + p\delta_{ij}]}{\partial x_j} = \frac{1}{Re}\frac{\partial \sigma_{ij}}{\partial x_j} + \mathcal{F}_i \tag{2.2}$$

$$\frac{\partial \varepsilon}{\partial t} + \frac{\partial [(\varepsilon + p)u_j]}{\partial x_j} = \frac{1}{\alpha}\frac{\partial}{\partial x_j}\left(\kappa_{tr}\frac{\partial T_{tr}}{\partial x_j} + \kappa_v \frac{\partial T_v}{\partial x_j}\right) + \frac{1}{Re}\frac{\partial (\sigma_{ij}u_i)}{\partial x_j} - \Lambda + \mathcal{F}_I + \mathcal{F}_j u_j \tag{2.3}$$

$$\frac{\partial E_v}{\partial t} + \frac{\partial (E_v u_j)}{\partial x_j} = \frac{1}{\alpha}\frac{\partial}{\partial x_j}\left(\kappa_v \frac{\partial T_v}{\partial x_j}\right) + \frac{E_v^* - E_v}{\tau_v} \tag{2.4}$$

$$p = \rho T_{tr}/(\gamma_r M^2) \tag{2.5}$$

where ρ, u_i, p, T_{tr} and T_v are the dimensionless density, velocity components, pressure, translational–rotational and vibrational temperatures, respectively. The total energy ε includes the kinetic energy ($\rho u_j u_j/2$), and the translational–rotational ($E_{tr} = 5\rho T_{tr}/(2\gamma_r M^2)$) and vibrational ($E_v$) energies. The dimensionless, large-scale forcings to the fluid momentum and the translational–rotational energy are respectively denoted as $\mathcal{F}_j$ and $\mathcal{F}_I$, which are explained in more detail in the appendix of Zheng *et al.* (2021). A spatially uniform thermal cooling function Λ is adopted to sustain the internal energy in a statistically steady state. In the equation of state (2.5), only the translational–rotational temperature T_{tr} is adopted since the pressure mainly stems from the translational motion of molecules rather than the rotational and vibrational motions (Vincenti & Kruger 1965). The reference Reynolds number $Re = \rho_r U_r L_r/\mu_r$, the reference Mach number $M = U_r/c_r$ and the reference Prandtl number $Pr = \mu_r C_{p_r}/\kappa_r$ are three governing parameters. Here, ρ_r, U_r, L_r and μ_r are respectively the reference density, velocity, length and viscosity coefficient. The reference speed of sound is given by $c_r = \sqrt{\gamma_r R T_r}$, where R is the specific

gas constant and $T_r = 1200\,\mathrm{K}$ is the reference temperature. The parameter $\gamma_r = C_{p_r}/C_{v_r}$ is the ratio of specific heat at constant pressure C_{p_r} to that at constant volume C_{v_r}, approximately equalling 1.324 according to the ratio of specific heats of dry air at $T_r = 1200\,\mathrm{K}$. The dimensionless parameter α is defined as $\alpha \equiv PrRe(\gamma_r - 1)M^2$, where Pr equals 0.71.

The vibrational energy per unit volume in equilibrium (E_v^*) and non-equilibrium (E_v) for diatomic molecules, and the viscosity stress σ_{ij} are given as

$$E_v^* = \frac{\rho\theta_v}{\gamma_r M^2[\exp(\theta_v/T_{tr}) - 1]}, \tag{2.6}$$

$$E_v = \frac{\rho\theta_v}{\gamma_r M^2[\exp(\theta_v/T_v) - 1]}, \tag{2.7}$$

and

$$\sigma_{ij} = \mu\left(\frac{\partial u_i}{\partial x_j} + \frac{\partial u_j}{\partial x_i}\right) - \frac{2}{3}\mu\theta\delta_{ij}. \tag{2.8}$$

The parameter θ_v is the characteristic vibrational temperature normalized by T_r, while $\theta = \partial u_k/\partial x_k$ is the velocity divergence. The temperature-dependent viscosity (μ) and thermal conductivity coefficients (κ_{tr} and κ_v) are specified by the Sutherland and Eucken laws (Vincenti & Kruger 1965; Anderson 2006). For their detailed expressions, please refer to our previous publication (Zheng *et al.* 2020).

The vibrational rate $Q_v = (E_v^* - E_v)/\tau_v$ in the vibrational energy governing equation (2.4) is based on the widely used Landau–Teller relaxation model. The dimensionless relaxation time (τ_v) relies closely on the local temperature and pressure, and is roughly calculated by

$$\tau_v = (C/p)\exp(K_2/T_{tr})^{1/3}. \tag{2.9}$$

Here, C and K_2 are dimensionless constants relating to the molecular structure of gases. In the current simulations, the dimensionless parameter $\langle K_\tau\rangle = \langle\tau_v\rangle/\tau_\eta$ is adopted to characterize the time scale of the relaxation process, where the $\langle\cdot\rangle$ operator stands for the spatial average. Also, $\tau_\eta = [\langle\mu/(Re\rho)\rangle/\epsilon]^{1/2}$ is the Kolmogorov time scale, and $\epsilon = \langle\sigma_{ij}\mathcal{S}_{ij}/Re\rangle/\langle\rho\rangle$ is the kinetic energy dissipation rate due to viscosity. The value of K_2 is set to be 2000.0, while the constant C is adjusted to obtain a specific $\langle K_\tau\rangle$ value.

The governing equations of compressible turbulence are numerically solved in a cubic box with a side length equalling 2π and a 512^3 grid resolution. Periodic boundary conditions are adopted in all three spatial directions. The hybrid compact-weighted essentially non-oscillatory (compact-WENO) scheme is applied, which couples a eighth-order central compact finite difference scheme in smooth regions with a seventh-order WENO scheme in shock regions (Lele 1992; Balsara & Shu 2000; Wang *et al.* 2010). The time derivative is approximated by the total variation diminishing (TVD) Runge–Kutta method (Gottlieb & Shu 1998). Following Samtaney, Pullin & Kosović (2001), the velocity field, which is divergence free, is initialized using a random field with a specified spectrum ($E(k) = 0.011k^4\exp(-k^2/8)$, where k is the wavenumber). Meanwhile, the normalized temperatures (T_{tr} and T_v) and density (ρ) are initialized with constant values (1.0) at all spatial points, and the initial pressure is determined from the equation of state (2.5). After the system reaches the statistically stationary state, 61 flow fields, uniformly spanning the time period of $9.01 \lesssim t/T_e \lesssim 14.41$, are adopted to obtain the statistical averages of quantities. Here, $T_e(=\sqrt{3}L_f/u')$ is the large eddy turnover time and L_f is the integral length scale.

2.2. *Forcing strategy*

The velocity field $\boldsymbol{u}(\boldsymbol{x}, t)$ is transformed into the wave space using the Fourier transform, and further decomposed into a solenoidal field ($\hat{\boldsymbol{u}}^S(\boldsymbol{k}, t)$) and a dilatational field ($\hat{\boldsymbol{u}}^D(\boldsymbol{k}, t)$) based on the Helmholtz decomposition, where $\boldsymbol{k}$ is the wave vector. The kinetic energy per unit mass for each wave vector is thus decomposed as follows:

$$\frac{|\hat{\boldsymbol{u}}(\boldsymbol{k}, t)|^2}{2} = \frac{|\hat{\boldsymbol{u}}^S(\boldsymbol{k}, t)|^2}{2} + \frac{|\hat{\boldsymbol{u}}^D(\boldsymbol{k}, t)|^2}{2}. \tag{2.10}$$

The kinetic energy in each of the first two wavenumber shells is calculated as

$$E^u(0.5 \le k < 1.5) = \sum_{0.5 \le |\boldsymbol{k}| < 1.5} \left(\frac{|\hat{\boldsymbol{u}}(\boldsymbol{k}, t)|^2}{2} \right), \tag{2.11}$$

and

$$E^u(1.5 \le k < 2.5) = \sum_{1.5 \le |\boldsymbol{k}| < 2.5} \left(\frac{|\hat{\boldsymbol{u}}(\boldsymbol{k}, t)|^2}{2} \right). \tag{2.12}$$

Similarly, the kinetic energy in the first two wavenumber shells is decomposed as

$$E^u(0.5 \le k < 1.5) = E^{u,S}(0.5 \le k < 1.5) + E^{u,D}(0.5 \le k < 1.5), \tag{2.13}$$

and

$$E^u(1.5 \le k < 2.5) = E^{u,S}(1.5 \le k < 2.5) + E^{u,D}(1.5 \le k < 2.5). \tag{2.14}$$

The large-scale momentum forcing is applied to the solenoidal velocity component, while the dilatational velocity component is left untouched (Petersen & Livescu 2010; Wang *et al.* 2010; Donzis & Jagannathan 2013). To maintain the total kinetic energy in the first two shells to the prescribed levels $E_u(1)$ and $E_u(2)$, respectively, the solenoidal velocity component is amplified. The forced velocity field $\hat{\boldsymbol{u}}^f(\boldsymbol{k}, t)$ is given as

$$\hat{\boldsymbol{u}}^f(\boldsymbol{k}, t) = \alpha \hat{\boldsymbol{u}}^S(\boldsymbol{k}, t) + \hat{\boldsymbol{u}}^D(\boldsymbol{k}, t), \tag{2.15}$$

where α for all modes in each wavenumber shell is set to be

$$\alpha(0.5 \le k < 1.5) = \sqrt{\frac{E^u(1) - E^{u,D}(0.5 \le k < 1.5)}{E^{u,S}(0.5 \le k < 1.5)}}, \tag{2.16}$$

and

$$\alpha(1.5 \le k < 2.5) = \sqrt{\frac{E^u(2) - E^{u,D}(1.5 \le k < 2.5)}{E^{u,S}(1.5 \le k < 2.5)}}, \tag{2.17}$$

where $E^u(1) = 1.242$ and $E^u(2) = 0.391$.

The large-scale thermal forcing for the translational–rotational temperature field is similar to that for the solenoidal velocity field (Donzis & Maqui 2016; Wang *et al.* 2019). The translational–rotational temperature field $T_{tr}(\boldsymbol{x}, t)$ is transformed into Fourier space to

yield $\hat{T}_{tr}(\boldsymbol{k}, t)$. Similarly,

$$E^{T_{tr}}(0.5 \leq k < 1.5) = \sum_{0.5 \leq |\boldsymbol{k}| < 1.5} (|\hat{T}_{tr}(\boldsymbol{k}, t)|^2), \tag{2.18}$$

and

$$E^{T_{tr}}(1.5 \leq k < 2.5) = \sum_{1.5 \leq |\boldsymbol{k}| < 2.5} (|\hat{T}_{tr}(\boldsymbol{k}, t)|^2). \tag{2.19}$$

The forced translational–rotational temperature is given as

$$\hat{T}^f_{tr}(\boldsymbol{k}, t) = \beta \hat{T}_{tr}(\boldsymbol{k}, t), \tag{2.20}$$

where β for all modes in each wavenumber shell is set to be

$$\beta(0.5 \leq k < 1.5) = \sqrt{\frac{E^{T_{tr}}(1)}{E^{T_{tr}}(0.5 \leq k < 1.5)}}, \tag{2.21}$$

and

$$\beta(1.5 \leq k < 2.5) = \sqrt{\frac{E^{T_{tr}}(2)}{E^{T_{tr}}(1.5 \leq k < 2.5)}}, \tag{2.22}$$

where $E^{T_{tr}}(1) = E^u(1)/100$ and $E^{T_{tr}}(2) = E^u(2)/100$.

In present simulations, the momentum and thermal forcings act on the large scales, and are expected to have a small impact on the statistics properties in the inertial regime. However, the large-scale thermal forcing in the present simulations cannot completely reproduce the shock-induced heating in the high-speed flows of practical interest.

3. Simulation parameters and one-point statistics

The overall statistics for the current simulations are summarized in tables 1–4. The reference Reynolds number (Re) equals 400, and the reference Mach numbers (M) are set to be 0.099 and 0.296. Three characteristic vibrational temperatures (θ_v = 1.0, 3.0 and 5.0) are employed. A smaller θ_v suggests an easier excitation for the vibrational mode. The spatially averaged ratio of the vibrational energy to the total internal energy (i.e. $\langle E^*_v/(E_{tr} + E^*_v)\rangle$) approximately equals 18.88 %, 5.92 % and 1.34 % with $\theta_v = 1.0$, 3.0 and 5.0, respectively. The Taylor microscale Reynolds number (Re_λ) and turbulent Mach number (M_t) are respectively defined as

$$Re_\lambda = Re\frac{\langle\rho\rangle u'\lambda}{\sqrt{3}\langle\mu\rangle}, \quad \text{and} \quad M_t = M\frac{u'}{\langle\sqrt{T_{tr}}\rangle}, \tag{3.1a,b}$$

where the root mean square (r.m.s.) value of velocity magnitude (u') and the Taylor microscale (λ) are respectively given as

$$u' = \sqrt{\langle u_1^2 + u_2^2 + u_3^2\rangle}, \tag{3.2}$$

and

$$\lambda = \sqrt{\frac{\langle u_1^2 + u_2^2 + u_3^2\rangle}{\langle(\partial u_1/\partial x_1)^2 + (\partial u_2/\partial x_2)^2 + (\partial u_3/\partial x_3)^2\rangle}}. \tag{3.3}$$

Case	Re	M	θ_v	Re_λ	M_t	$\langle K_\tau \rangle$	$\eta/\Delta x$	θ'	$\langle \omega^2 \rangle$	$\langle D^D_{ij} D^D_{ij} \rangle$	$\langle D^S_{ij} D^S_{ij} \rangle$
I_1	400	0.099	1.0	155.5	0.22	0.16	1.04	0.91	290.0	0.55	144.9
I_2	400	0.099	1.0	158.4	0.22	0.77	1.04	0.58	277.5	0.23	138.7
I_3	400	0.099	1.0	155.9	0.22	4.00	1.04	0.56	286.1	0.22	143.0
I_4	400	0.099	1.0	160.2	0.22	9.80	1.05	1.53	243.6	1.68	121.8
I_5	400	0.099	1.0	156.2	0.22	741.4	1.07	3.63	236.4	8.80	118.2

Table 1. Simulation parameters and resulting flow statistics for compressible turbulence with $M_t \approx 0.22$. Considering effects of $\langle K_\tau \rangle$.

Case	Re	M	θ_v	Re_λ	M_t	$\langle K_\tau \rangle$	$\eta/\Delta x$	θ'	$\langle \omega^2 \rangle$	$\langle D^D_{ij} D^D_{ij} \rangle$	$\langle D^S_{ij} D^S_{ij} \rangle$
I_2	400	0.099	1.0	158.4	0.22	0.77	1.04	0.58	277.5	0.23	138.7
I_6	400	0.099	3.0	157.7	0.22	0.84	1.06	1.09	261.2	0.81	130.5
I_7	400	0.099	5.0	158.1	0.22	0.82	1.06	1.78	262.1	2.15	131.0

Table 2. Simulation parameters and resulting flow statistics for compressible turbulence with $M_t \approx 0.22$. Considering effects of θ_v.

Case	Re	M	θ_v	Re_λ	M_t	$\langle K_\tau \rangle$	$\eta/\Delta x$	θ'	$\langle \omega^2 \rangle$	$\langle D^D_{ij} D^D_{ij} \rangle$	$\langle D^S_{ij} D^S_{ij} \rangle$
II_1	400	0.296	1.0	153.4	0.68	0.19	1.01	2.50	313.4	4.16	156.6
II_2	400	0.296	1.0	159.6	0.68	0.86	1.04	2.10	275.7	2.94	137.8
II_3	400	0.296	1.0	160.6	0.66	4.27	1.06	1.67	250.3	1.68	125.1
II_4	400	0.296	1.0	151.9	0.68	9.98	1.01	2.59	301.8	4.44	150.9
II_5	400	0.296	1.0	154.2	0.68	931.0	1.03	3.40	277.1	7.71	138.5

Table 3. Simulation parameters and resulting flow statistics for compressible turbulence with $M_t \approx 0.68$. Considering effects of $\langle K_\tau \rangle$.

Case	Re	M	θ_v	Re_λ	M_t	$\langle K_\tau \rangle$	$\eta/\Delta x$	θ'	$\langle \omega^2 \rangle$	$\langle D^D_{ij} D^D_{ij} \rangle$	$\langle D^S_{ij} D^S_{ij} \rangle$
II_2	400	0.296	1.0	159.6	0.68	0.86	1.04	2.10	275.7	2.94	137.8
II_6	400	0.296	3.0	154.0	0.68	0.97	1.01	2.57	303.4	4.40	151.6
II_7	400	0.296	5.0	155.1	0.67	0.91	1.03	2.95	276.5	5.77	138.2

Table 4. Simulation parameters and resulting flow statistics for compressible turbulence with $M_t \approx 0.68$. Considering effects of θ_v.

Here, M_t roughly equals 0.22 and 0.68 for the $M = 0.099$ and 0.296 cases, respectively, while Re_λ is approximately 157.5 (tables 1–4). The value of $\langle K_\tau \rangle$ approximately equals 0.16–741.4 for the $M = 0.099$ cases, and 0.19–931.0 for the $M = 0.296$ cases. In the present simulations, cases I_1–I_5 and II_1–II_5 are used to discuss the effect of $\langle K_\tau \rangle$, while cases I_2, I_6, I_7 and cases II_2, II_6, II_7 are adopted to study the effect of θ_v. Note that cases I_5 and II_5 can be approximately treated as frozen flow (Knisely & Zhong 2020) since their vibrational relaxation times are significantly larger than the Kolmogorov time scale (i.e. $\langle K_\tau \rangle \gg 1.0$). In the tables of this article, cases I_3, I_5 and I_7, as well as cases II_3, II_5 and II_7, are marked with colours as typical cases for easy comparison.

As presented in tables 1–4, the resolution parameter $\eta/\Delta x$ is in the range of $1.01 \lesssim \eta/\Delta x \lesssim 1.07$, where η is the Kolmogorov length scale and Δx is the grid spacing in each direction. The resolution parameter $k_{max}\eta$ is therefore in the range of $3.18 \lesssim k_{max}\eta \lesssim 3.37$, where the largest wavenumber k_{max} is half of the number of grid points in each direction. According to previous grid refinement studies (Wang *et al.* 2011, 2012), the grid resolutions with $k_{max}\eta \geq 2.77$ is enough for the convergence of the flow statistics.

The r.m.s. value of the velocity divergence (θ') is used to characterize the flow compressibility. The greater the θ', the stronger the flow compressibility. For the $M_t \approx 0.22$ cases (tables 1–2), θ' decreases from 0.91 to 0.56 as $\langle K_\tau \rangle$ increases from 0.16 to 4.00, and sharply increases to 3.63 with $\langle K_\tau \rangle \approx 741.4$; θ' increases from 0.58 to 1.78 with θ_v varying from 1.0 to 5.0. Similarly, for the $M_t \approx 0.68$ cases (tables 3–4), θ' decreases from 2.50 to 1.67 as $\langle K_\tau \rangle$ increases from 0.19 to 4.27, and increases to 3.40 with $\langle K_\tau \rangle \approx 931.0$; θ' increases from 2.10 to 2.95 with θ_v varying from 1.0 to 5.0. As revealed in Zheng *et al.* (2021), the large-scale thermal forcing enhances the flow compressibility, while the vibrational relaxation weakens it. From tables 1–4, cases I_3 and II_3 have the weakest compressibility, which suggests that they have the strongest relaxation level.

The instantaneous contours of θ/θ' with four typical cases (I_3, I_5, II_3 and II_5) in figure 1 and the PDFs of θ/θ' in figure 2 show a balance between the vibrational relaxation and the large-scale thermal forcing. One can see consistent results with tables 1–4. For the $M_t \approx 0.22$ cases, when the relaxation effect is significant (e.g. case I_3), the large-scale thermal forcing cannot strongly enhance the flow compressibility; no clear shocklet structure can be observed in the flow field (figure 1*a*) and the PDF of θ/θ' is almost symmetrical about the $\theta/\theta' = 0.0$ axis (figure 2*a*). As the relaxation effect fades (e.g. case I_5), the large-scale thermal forcing significantly enhances the flow compressibility; the clear shocklet structures lie across the flow field (figure 1*b*), and the PDF of θ/θ' is thus strongly skewed to the negative side (figure 2*a*). However, in comparison with the $M_t \approx 0.22$ cases, the large-scale thermal forcing and vibration relaxation have a weaker impact on the flow compressibility for the $M_t \approx 0.68$ cases, although similar phenomena are observed. The flow compressibility for case II_5 is obviously stronger than that of case II_3. For case II_5, the shocklet structures are more clear (figure 1*c*,*d*) and there is a stronger tendency for the PDF of θ/θ' to be skewed to a negative value (figure 2*b*). In order to clarify possible similarities to incompressible turbulence, the component of the strain tensor S_{ij} $(= (\partial u_i/\partial x_j + \partial u_j/\partial x_i)/2)$ is separated into the deviatoric strain-rate term D_{ij} $(= S_{ij} - S_{kk}\delta_{ij}/3)$ and the isotropic dilatational term $-S_{kk}\delta_{ij}/3$ (Erlebacher & Sarkar 1993). Based on the Helmholtz decomposition, D_{ij} can be further decomposed into the solenoidal and dilatational components, i.e. $D_{ij} = D^S_{ij} + D^D_{ij}$, where $D^S_{ij} = (\partial u^S_i/\partial x_j + \partial u^S_j/\partial x_i)/2$ and $D^D_{ij} = (\partial u^D_i/\partial x_j + \partial u^D_j/\partial x_i)/2 - \theta\delta_{ij}/3$. The solenoidal velocity component $\boldsymbol{u}^S$ satisfies $\boldsymbol{\nabla} \cdot \boldsymbol{u}^S = 0$, while the dilatational velocity component $\boldsymbol{u}^D$ follows $\boldsymbol{\nabla} \times \boldsymbol{u}^D = 0$.

As shown in tables 1–4, the dependence of $\langle D^D_{ij} D^D_{ij} \rangle$ on the vibrational relaxation behaves quite similar to θ', being smaller when the relaxation effect is significant (i.e. cases I_3 and II_3). For instance, $\langle D^D_{ij} D^D_{ij} \rangle$ decreases from 0.55 to 0.22 as $\langle K_\tau \rangle$ increases from 0.16 to 4.00, and jumps to 8.80 with $\langle K_\tau \rangle \approx 741.4$ ($M_t \approx 0.22$ cases, table 1). Similarly, variations of $\langle \omega^2 \rangle$ and $\langle D^S_{ij} D^S_{ij} \rangle$ are consistent with each other. Here, the vorticity is defined as $\boldsymbol{\omega} = \boldsymbol{\nabla} \times \boldsymbol{u}$ and $\langle \omega^2 \rangle = \langle \omega_1^2 + \omega_2^2 + \omega_3^2 \rangle$. However, the variation of $\langle \omega^2 \rangle$ (or $\langle D^S_{ij} D^S_{ij} \rangle$) is independent of the dilatation and vibrational relaxation.

Erlebacher & Sarkar (1993) mentioned that, in compressible homogeneous turbulence, the dilatation is statistically independent of the vorticity and variables constructed from the solenoidal velocity component. The statistical correlation between two parameters (i.e. f

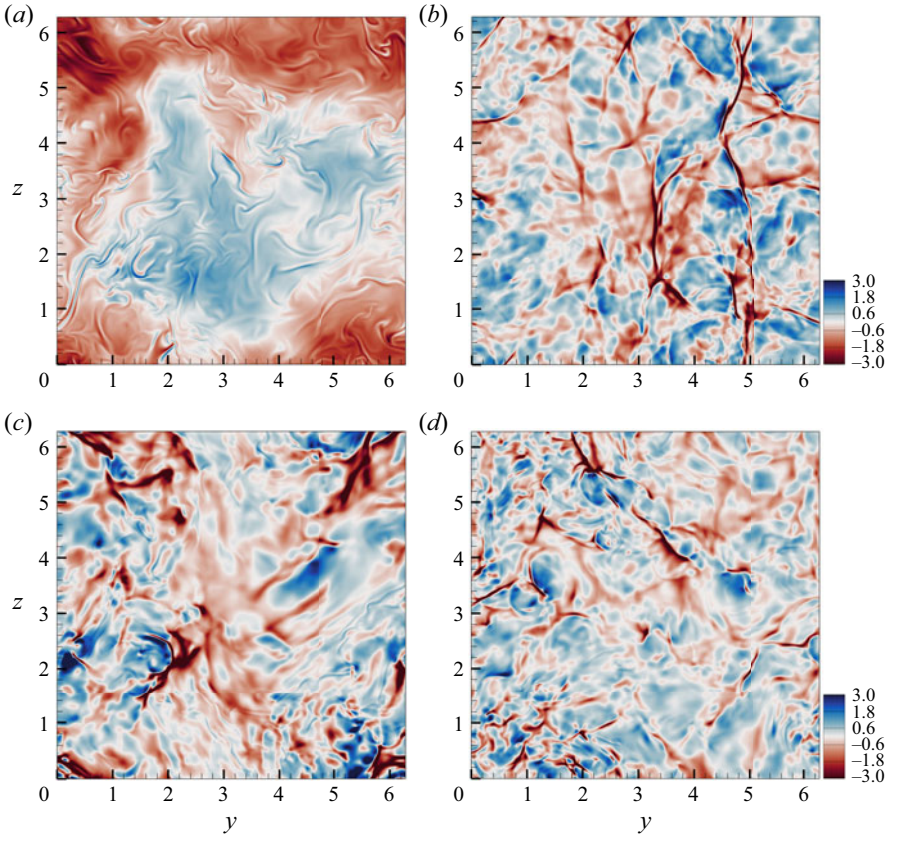

Figure 1. Instantaneous contours of normalized dilatation (θ/θ'). (*a*) Case I_3, (*b*) case I_5, (*c*) case II_3, (*d*) case II_5. Here, $x = 3.14$.

and g) can be estimated by their correlation coefficient

$$\mathrm{Corr}(f, g) = \frac{\langle (f - \langle f \rangle)(g - \langle g \rangle) \rangle}{\sqrt{\langle (f - \langle f \rangle)^2 \rangle \langle (g - \langle g \rangle)^2 \rangle}}. \tag{3.4}$$

The corresponding correlation coefficients for the $M_t \approx 0.22$ and $M_t \approx 0.68$ cases are given in tables 5 and 6. For the $M_t \approx 0.22$ cases (table 5), the small $\mathrm{Corr}(\theta^2, \omega^2)$, $\mathrm{Corr}(\theta^2, D_{ij}^S D_{ij}^S)$ and $\mathrm{Corr}(\omega^2, D_{ij}^D D_{ij}^D)$ for different cases (<0.14) suggest a weak correlation between the dilatation and the vorticity or the solenoidal component of the deviatoric strain-rate tensor, as well as that between the vorticity and the dilatational component of the deviatoric strain-rate tensor. However, for cases with a significant relaxation effect (i.e. cases I_1–I_3, especially case I_3), the correlation coefficients are larger than the other cases. For compressible turbulence without considering the relaxation effect, the correlation coefficients between the dilatation and any variables constructed from the solenoidal velocity component are less than 0.01 (Erlebacher & Sarkar 1993). However, in the current simulations, $\mathrm{Corr}(\theta^2, D_{ij}^S D_{ij}^S) \approx 0.137$ for case I_3, suggesting that the correlation between the dilatation and the solenoidal component of the deviatoric strain-rate tensor is enhanced by the relaxation effect. Similarly, the relaxation effect weakens the correlation between the dilatation and the dilatational component of the

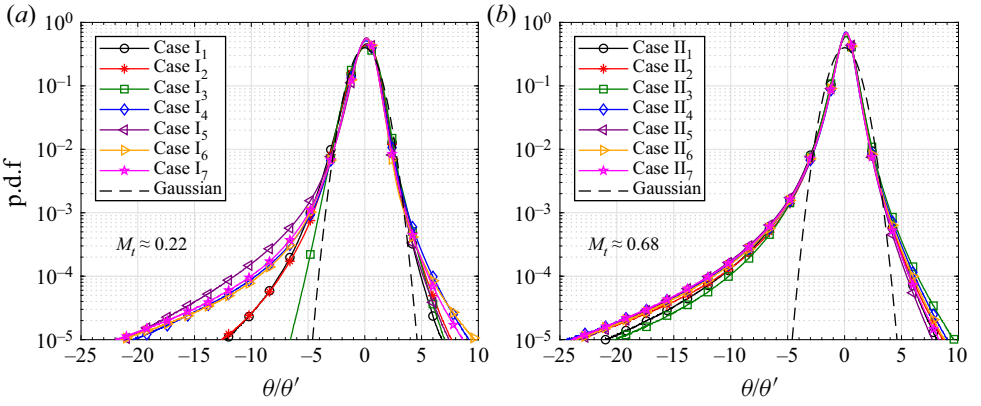

Figure 2. PDFs of normalized dilatation for the (*a*) $M_t \approx 0.22$ and (*b*) $M_t \approx 0.68$ cases.

Case	Corr(θ^2, ω^2)	Corr(θ^2, $D^S_{ij}D^S_{ij}$)	Corr(θ^2, $D^D_{ij}D^D_{ij}$)	Corr(ω^2, $D^S_{ij}D^S_{ij}$)	Corr(ω^2, $D^D_{ij}D^D_{ij}$)
I_1	0.026	0.053	0.662	0.530	0.045
I_2	0.039	0.099	0.542	0.523	0.056
I_3	0.060	0.137	0.285	0.530	0.094
I_4	0.004	0.007	0.948	0.519	0.007
I_5	0.009	0.013	0.948	0.526	0.013
I_6	0.011	0.020	0.934	0.534	0.015
I_7	0.009	0.014	0.941	0.534	0.012

Table 5. Correlation coefficients between some pairs of variables; $M_t \approx 0.22$.

Case	Corr(θ^2, ω^2)	Corr(θ^2, $D^S_{ij}D^S_{ij}$)	Corr(θ^2, $D^D_{ij}D^D_{ij}$)	Corr(ω^2, $D^S_{ij}D^S_{ij}$)	Corr(ω^2, $D^D_{ij}D^D_{ij}$)
II_1	0.011	0.010	0.919	0.612	0.037
II_2	0.008	0.008	0.937	0.612	0.027
II_3	0.013	0.014	0.921	0.592	0.038
II_4	0.013	0.011	0.924	0.608	0.035
II_5	0.013	0.011	0.920	0.604	0.032
II_6	0.014	0.013	0.923	0.605	0.039
II_7	0.013	0.012	0.923	0.612	0.033

Table 6. Correlation coefficients between some pairs of variables; $M_t \approx 0.68$.

deviatoric strain-rate tensor. The value of Corr(θ^2, $D^D_{ij}D^D_{ij}$) ≈ 0.662 with $\langle K_\tau \rangle \approx 0.16$, and sharply reduces to 0.285 with $\langle K_\tau \rangle \approx 4.00$. For cases I_4–I_7, where the relaxation effect fades, Corr(θ^2, $D^D_{ij}D^D_{ij}$) ≈ 0.943. Interestingly, Corr(ω^2, $D^S_{ij}D^S_{ij}$) is almost not affected by the vibrational relaxation, $\approx$0.528 (table 5).

For the $M_t \approx 0.68$ cases (table 6), Corr(θ^2, ω^2) $\approx$ Corr(θ^2, $D^S_{ij}D^S_{ij}$) ≈ 0.012, indicating that the dilatation is nearly uncorrelated with the vorticity and the solenoidal component of the deviatoric strain-rate tensor. Similarly, Corr(ω^2, $D^D_{ij}D^D_{ij}$) ≈ 0.034. However, θ^2 (or ω^2) strongly correlates with $D^D_{ij}D^D_{ij}$ (or $D^S_{ij}D^S_{ij}$), where Corr(θ^2, $D^D_{ij}D^D_{ij}$) ≈ 0.924 and Corr(ω^2, $D^S_{ij}D^S_{ij}$) ≈ 0.606. Furthermore, the correlation between the dilatation (or

vorticity) and the dilatational (or solenoidal) component of the deviatoric strain-rate tensor is nearly not affected by the vibrational relaxation (table 6). To quantify the effects of dilatation, the flow region is divided into six subregions based on the local dilatational level: (i) strong compression region with $\theta/\theta' \in (-\infty, -2.0]$; (ii) moderate compression region with $\theta/\theta' \in (-2.0, -1.0]$; (iii) weak compression region with $\theta/\theta' \in (-1.0, 0.0]$; (iv) weak expansion region with $\theta/\theta' \in (0.0, 1.0]$; (v) moderate expansion region with $\theta/\theta' \in (1.0, 2.0]$; (vi) strong expansion region with $\theta/\theta' \in (2.0, +\infty)$. Figure 3 presents the averages of the normalized magnitude of the vorticity and deviatoric strain-rate components conditioned on the local dilatation. For the $M_t \approx 0.22$ cases, conditional averages of $\omega^2/\langle\omega^2\rangle$ and $D_{ij}^S D_{ij}^S/\langle D_{ij}^S D_{ij}^S\rangle$ have similar behaviours (figure 3*a*,*b*). When the relaxation effect is significant (e.g. cases I_1–I_3), as revealed in table 5, the correlation between the dilatation and vorticity (as well as the solenoidal component of the deviatoric strain-rate tensor) is stronger than the other cases. Consequently, the conditional averages of $\omega^2/\langle\omega^2\rangle$ and $D_{ij}^S D_{ij}^S/\langle D_{ij}^S D_{ij}^S\rangle$ increase sharply in the strong expansion region. Similarly, they increase with the local dilatational level in the strong compression region. However, the growth rate for case I_3 is obviously larger than the other two cases. For the cases with a weak relaxation effect (e.g. cases I_4–I_7), the conditional averages of $\omega^2/\langle\omega^2\rangle$ and $D_{ij}^S D_{ij}^S/\langle D_{ij}^S D_{ij}^S\rangle$ approach 1.0 in the compression region, and increase slightly in the expansion region. In figure 3(*c*), the conditional average of $D_{ij}^D D_{ij}^D/\langle D_{ij}^D D_{ij}^D\rangle$ approaches zero at $\theta/\theta' = 0.0$, and increases with the local dilatational level in both compression and expansion regions. As the flow compressibility for cases I_1–I_3 is weakened by the relaxation effect, the conditional averages of $D_{ij}^D D_{ij}^D/\langle D_{ij}^D D_{ij}^D\rangle$ for these cases are thus smaller than other cases with identical dilatational levels. Note that, in figure 3(*a*–*c*), the lines fluctuate irregularly in the ranges of $\theta/\theta' < -5.0$ and $\theta/\theta' > 5.0$, especially for cases I_1–I_3. This observation can be attributed to the insufficient data in these ranges due to the weak dilatation, as shown in figure 2.

For the $M_t \approx 0.68$ cases, the conditional averages of $\omega^2/\langle\omega^2\rangle$ and $D_{ij}^S D_{ij}^S/\langle D_{ij}^S D_{ij}^S\rangle$ are almost constant, being nearly independent of the local dilatation in the strong compression region (figure 3*d*,*e*). They decrease slightly in the range of $-2.0 \leq \theta/\theta' \leq 0.0$, and increase monotonically in the expansion region. Meanwhile, the conditional average of $D_{ij}^D D_{ij}^D/\langle D_{ij}^D D_{ij}^D\rangle$ rises with the local dilatation in both compression and expansion regions (figure 3*f*). Effects of vibrational relaxation on the conditional averages of $\omega^2/\langle\omega^2\rangle$, $D_{ij}^D D_{ij}^D/\langle D_{ij}^D D_{ij}^D\rangle$ and $D_{ij}^S D_{ij}^S/\langle D_{ij}^S D_{ij}^S\rangle$ are negligible; the lines corresponding to different cases almost overlap each other. These observations agree with the results in table 6.

4. Enstrophy production

4.1. *Dilatational effect on enstrophy production*

From the vorticity transport equation, the governing equation for enstrophy ($\omega^2/2$) can be derived as follows (Wang *et al.* 2011; Papapostolou *et al.* 2017):

$$\left(\frac{\partial}{\partial t} + u_j\frac{\partial}{\partial x_j}\right)\frac{\omega^2}{2} = \omega_i\omega_j S_{ij} - \omega^2\theta + \omega_i\frac{\epsilon_{ijk}}{\rho^2}\frac{\partial\rho}{\partial x_j}\frac{\partial p}{\partial x_k} + \omega_i\frac{\epsilon_{ijk}}{Re}\frac{\partial}{\partial x_j}\left(\frac{1}{\rho}\frac{\partial\sigma_{mk}}{\partial x_m}\right) + \omega_i\epsilon_{ijk}\frac{\partial\mathcal{F}_k}{\partial x_j}. \tag{4.1}$$

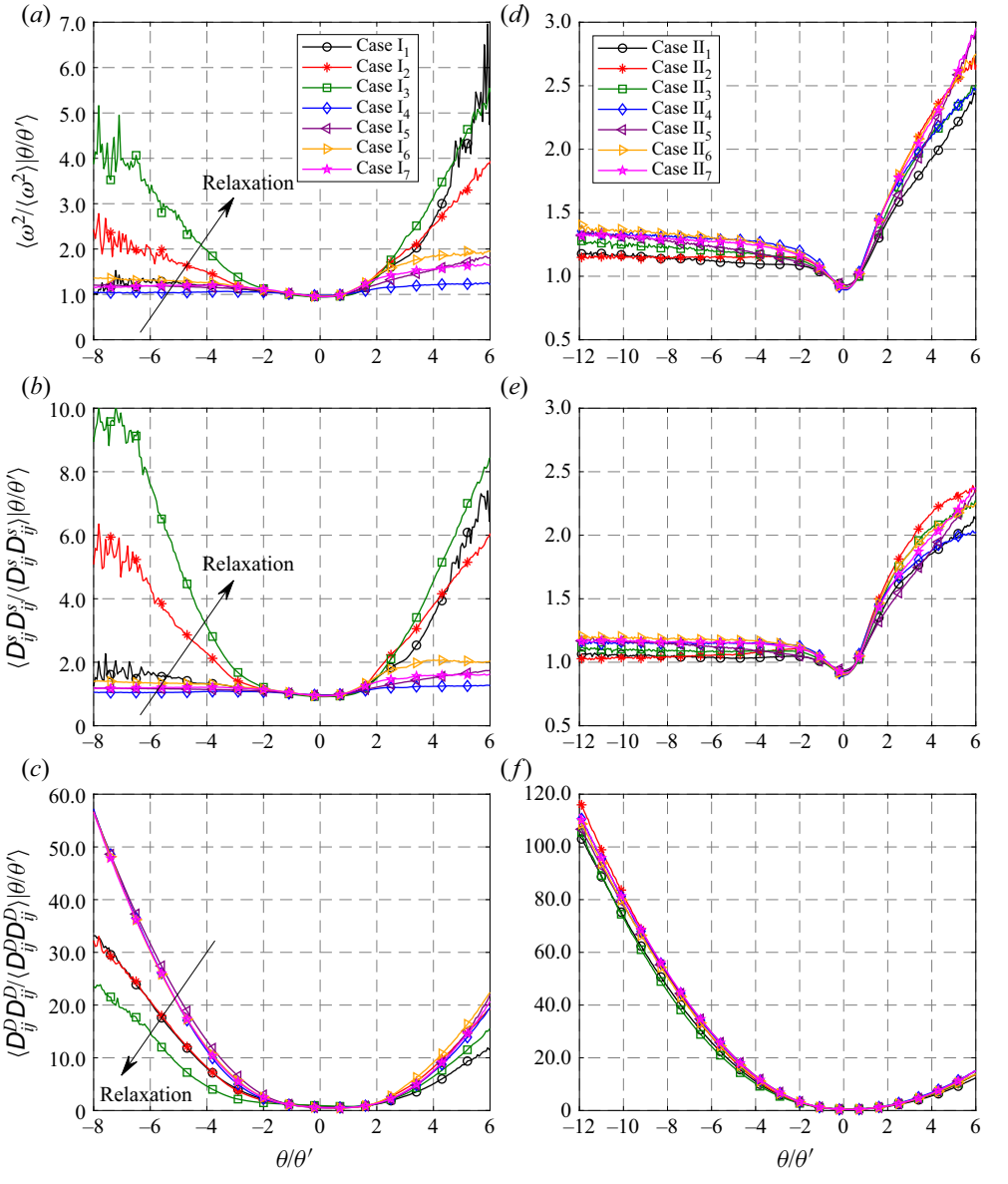

Figure 3. Conditional averages of the normalized magnitudes of the vorticity and deviatoric strain-rate components; (*a*,*d*) $\langle \omega^2/\langle\omega^2\rangle \mid \theta/\theta'\rangle$, (*b*,*e*) $\langle D_{ij}^S D_{ij}^S/\langle D_{ij}^S D_{ij}^S\rangle \mid \theta/\theta'\rangle$ and (*c*,*f*) $\langle D_{ij}^D D_{ij}^D/\langle D_{ij}^D D_{ij}^D\rangle \mid \theta/\theta'\rangle$. For (*a–c*) $M_t \approx 0.22$ and (*d–f*) $M_t \approx 0.68$.

In (4.1), $P_\omega = \omega_i\omega_j S_{ij}$ is the vortex stretching and tilting (strain) term, $D_\omega = -\omega^2\theta$ is the dilatational term, $B_\omega = (1/\rho^2)\varepsilon_{ijk}\omega_i(\partial\rho/\partial x_j)(\partial p/\partial x_j)$ is the baroclinic term, $V_\omega = (1/Re)\omega_i\epsilon_{ijk}(\partial/\partial x_j)(\partial\sigma/\partial x_m)$ is the viscous term and $F_\omega = \omega_i\epsilon_{ijk}(\partial\mathcal{F}_k/\partial x_j)$ is the large-scale forcing term. The parameter F_ω is expected to have a small impact on the local enstrophy production because the momentum forcing is at large scales. The local enstrophy production thus mainly includes contributions from the strain, dilatational and baroclinic effects. However, the contribution from the baroclinic term is negligible in

Case	$\mathcal{F}(S_{ij}^*)$	$\mathcal{F}(D_{ij}^S)$	$\mathcal{F}(D_{ij}^D)$	$\mathcal{F}(-\theta/6)$	Case	$\mathcal{F}(S_{ij}^*)$	$\mathcal{F}(D_{ij}^S)$	$\mathcal{F}(D_{ij}^D)$	$\mathcal{F}(-\theta/6)$
I_1	824.1	826.1	−0.65	−0.80	II_1	908.4	914.9	−2.26	−3.72
I_2	745.0	745.4	0.13	−0.30	II_2	750.5	755.6	−1.40	−3.38
I_3	801.6	803.6	−1.04	−0.57	II_3	642.8	647.4	−2.04	−2.36
I_4	609.7	609.8	0.44	−0.36	II_4	862.6	869.4	−3.43	−3.05
I_5	589.2	587.9	1.59	−0.05	II_5	757.9	760.7	0.16	−2.70
I_6	702.8	703.8	−0.07	−0.45	II_6	864.5	869.5	−1.36	−3.18
I_7	700.8	701.4	0.36	−0.57	II_7	763.5	768.3	−1.72	−2.72

Table 7. Spatial averages of the net enstrophy production and its components; $\mathcal{F}(S_{ij}^*) = \langle \omega_i\omega_j S_{ij}^* \rangle$, $\mathcal{F}(D_{ij}^S) = \langle \omega_i\omega_j D_{ij}^S \rangle$, $\mathcal{F}(D_{ij}^D) = \langle \omega_i\omega_j D_{ij}^D \rangle$ and $\mathcal{F}(-\theta/6) = \langle -\omega^2\theta/6 \rangle$.

compressible isotropic turbulence (Wang *et al.* 2011). The specific focus in the current analysis is therefore on the strain and dilatational terms.

Equation (4.1) can be further derived as

$$\frac{\partial(\omega^2/2)}{\partial t} + \frac{\partial(u_j\omega^2/2)}{\partial x_j} = \omega_i\omega_j S_{ij}^* + \omega_i \frac{\epsilon_{ijk}}{\rho^2}\frac{\partial\rho}{\partial x_j}\frac{\partial p}{\partial x_k} + \omega_i \frac{\epsilon_{ijk}}{Re}\frac{\partial}{\partial x_j}\left(\frac{1}{\rho}\frac{\partial\sigma_{mk}}{\partial x_m}\right) + \omega_i\epsilon_{ijk}\frac{\partial\mathcal{F}_k}{\partial x_j}, \tag{4.2}$$

where the component of the modified strain-rate tensor $S_{ij}^* = S_{ij} - S_{kk}\delta_{ij}/2 = D_{ij} - S_{kk}\delta_{ij}/6$. The net enstrophy production term $(\omega_i\omega_j S_{ij}^*)$ thus can be rewritten as

$$\omega_i\omega_j S_{ij}^* = \omega_i\omega_j D_{ij}^S + \omega_i\omega_j D_{ij}^D - \frac{1}{6}\theta\omega^2. \tag{4.3}$$

The spatial averages of the net enstrophy production and its components for the $M_t \approx 0.22$ and 0.68 cases are listed in table 7. It is clearly observed that $\langle \omega_i\omega_j S_{ij}^* \rangle \approx \langle \omega_i\omega_j D_{ij}^S \rangle$, while $\langle \omega_i\omega_j D_{ij}^D \rangle$ and $\langle -(1/6)\theta\omega^2 \rangle$ are negligible. This indicates that, from the full flow field perspective, the enstrophy production mainly stems from the solenoidal component of the deviatoric strain-rate tensor. However, there is no obvious relationship between the spatial averages of the net enstrophy production (or its components) and the vibrational relaxation. Figure 4 illustrates the instantaneous contours of ω/ω', $\omega_i\omega_j D_{ij}^S/\langle \omega_i\omega_j S_{ij}^* \rangle$, $\omega_i\omega_j D_{ij}^D/\langle \omega_i\omega_j S_{ij}^* \rangle$ and $-(1/6)\omega^2\theta/\langle \omega_i\omega_j S_{ij}^* \rangle$ for case I_5. While the correlation coefficients between vorticity and different enstrophy production terms (including their absolute values) are listed in table 8. It is found that the structures of the vorticity (ω/ω') and enstrophy production terms $(\omega_i\omega_j D_{ij}^S/\langle \omega_i\omega_j S_{ij}^* \rangle$, $\omega_i\omega_j D_{ij}^D/\langle \omega_i\omega_j S_{ij}^* \rangle$ and $-(1/6)\omega^2\theta/\langle \omega_i\omega_j S_{ij}^* \rangle)$ are similar, for example, as marked by the circles with a dashed line. Consequently, the vorticity has a strong correlation with the absolute values of the enstrophy production terms. The correlation coefficients are larger than 0.53 (table 8). On the other hand, unlike the global averages in table 7, the local magnitudes of $\omega_i\omega_j D_{ij}^D/\langle \omega_i\omega_j S_{ij}^* \rangle$ and $-(1/6)\omega^2\theta/\langle \omega_i\omega_j S_{ij}^* \rangle$ can be considerable, especially for cases with a weak relaxation effect (e.g. case I_5, figure 4*c*,*d*). However, the positive values in the compression region and the negative values in the expansion region cancel out on average, leading to a negligible amount. This is why $\mathrm{Corr}(\omega/\omega', \mathcal{W}(D_{ij}^D))$ and $\mathrm{Corr}(\omega/\omega', \mathcal{W}(-\theta/6))$ are close to zero (table 8).

Figures 5 and 6 present the spatial averages of $\omega_i\omega_j S_{ij}^*/\langle \omega_i\omega_j S_{ij}^* \rangle$, $\omega_i\omega_j D_{ij}^D/\langle \omega_i\omega_j S_{ij}^* \rangle$, $\omega_i\omega_j D_{ij}^S/\langle \omega_i\omega_j S_{ij}^* \rangle$ and $-(1/6)\theta\omega^2/\langle \omega_i\omega_j S_{ij}^* \rangle$ conditioned on the local dilatation for the

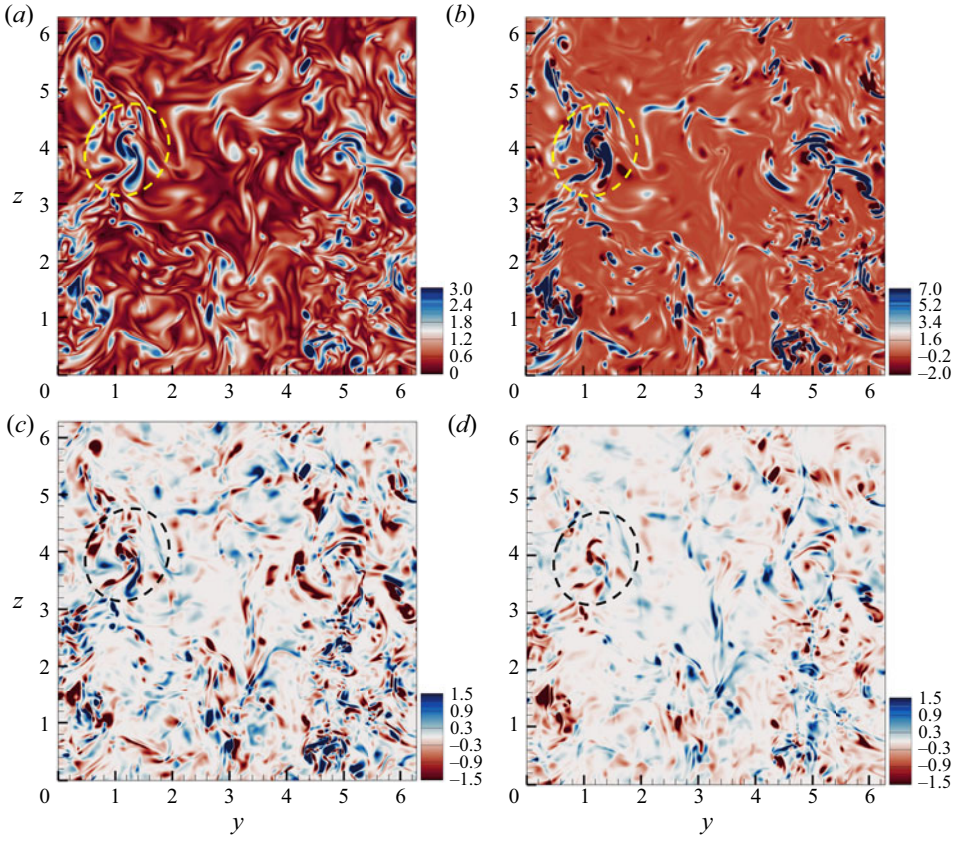

Figure 4. Instantaneous contours of (*a*) ω/ω', (*b*) $\omega_i\omega_j D^S_{ij}/\langle\omega_i\omega_j S^*_{ij}\rangle$, (*c*) $\omega_i\omega_j D^D_{ij}/\langle\omega_i\omega_j S^*_{ij}\rangle$, (*d*) $-(1/6)\omega^2\theta/\langle\omega_i\omega_j S^*_{ij}\rangle$. Here, $x = 3.14$ and $\omega' = \sqrt{\langle\omega_1^2+\omega_2^2+\omega_3^2\rangle}$. Case I_5.

$\mathrm{Corr}(\omega/\omega', \mathcal{W}(S^*_{ij}))$	$\mathrm{Corr}(\omega/\omega', \mathcal{W}(D^S_{ij}))$	$\mathrm{Corr}(\omega/\omega', \mathcal{W}(D^D_{ij}))$	$\mathrm{Corr}(\omega/\omega', \mathcal{W}(-\theta/6))$
0.493	0.510	0.006	−0.003
$\mathrm{Corr}(\omega/\omega', \lvert\mathcal{W}(S^*_{ij})\rvert)$	$\mathrm{Corr}(\omega/\omega', \lvert\mathcal{W}(D^S_{ij})\rvert)$	$\mathrm{Corr}(\omega/\omega', \lvert\mathcal{W}(D^D_{ij})\rvert)$	$\mathrm{Corr}(\omega/\omega', \lvert\mathcal{W}(-\theta/6)\rvert)$
0.618	0.622	0.531	0.535

Table 8. Correlation coefficients between vorticity and enstrophy production terms (including their absolute values). Case I_5; $\mathcal{W}(S^*_{ij}) = \omega_i\omega_j S^*_{ij}/\langle\omega_i\omega_j S^*_{ij}\rangle$, $\mathcal{W}(D^S_{ij}) = \omega_i\omega_j D^S_{ij}/\langle\omega_i\omega_j S^*_{ij}\rangle$, $\mathcal{W}(D^D_{ij}) = \omega_i\omega_j D^D_{ij}/\langle\omega_i\omega_j S^*_{ij}\rangle$ and $\mathcal{W}(-\theta/6) = (-\omega^2\theta/6)/\langle\omega_i\omega_j S^*_{ij}\rangle$.

$M_t \approx 0.22$ and 0.68 cases, respectively. As illustrated in figure 5(*a*), the conditional averages of $\omega_i\omega_j S^*_{ij}/\langle\omega_i\omega_j S^*_{ij}\rangle$ among the $M_t \approx 0.22$ cases are very different from each other. The conditional averages of $\omega_i\omega_j S^*_{ij}/\langle\omega_i\omega_j S^*_{ij}\rangle$ approximately equal 1.0 at $\theta/\theta' = 0.0$. When the relaxation effect is significant (e.g. cases I_1–I_3), the conditional averages of $\omega_i\omega_j S^*_{ij}/\langle\omega_i\omega_j S^*_{ij}\rangle$ increase in the strong expansion and compression regions, and case I_3 exhibits the largest growth rate. For cases with a weak relaxation effect (e.g. cases I_4–I_7), the conditional averages of $\omega_i\omega_j S^*_{ij}/\langle\omega_i\omega_j S^*_{ij}\rangle$ increase slightly in the compression

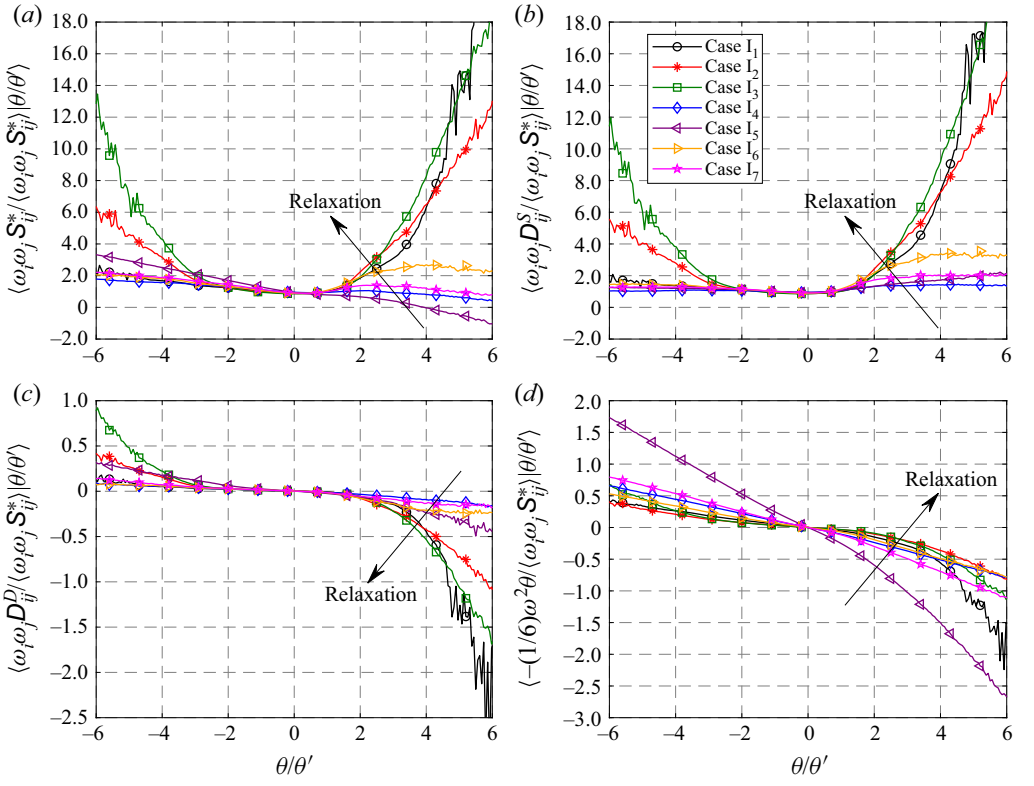

Figure 5. Conditional averages of the net enstrophy production and its components; (*a*) $\langle \omega_i\omega_j S^*_{ij}/\langle \omega_i\omega_j S^*_{ij}\rangle \mid \theta/\theta'\rangle$, (*b*) $\langle \omega_i\omega_j D^S_{ij}/\langle \omega_i\omega_j S^*_{ij}\rangle \mid \theta/\theta'\rangle$, (*c*) $\langle \omega_i\omega_j D^D_{ij}/\langle \omega_i\omega_j S^*_{ij}\rangle \mid \theta/\theta'\rangle$ and (*d*) $\langle -(1/6)\omega^2\theta/\langle \omega_i\omega_j S^*_{ij}\rangle \mid \theta/\theta'\rangle$. Here, $M_t \approx 0.22$.

region, and gradually change from increasing to decreasing in the expansion region as the relaxation effect fades. For instance, the conditional average of $\omega_i\omega_j S^*_{ij}/\langle \omega_i\omega_j S^*_{ij}\rangle$ for case I_5 decreases from 1.0 to 0.0 in the range of $0.0 \leq \theta/\theta' \leq 4.0$, and is negative at $\theta/\theta' > 4.0$. In figure 5(*b*), the conditional averages of $\omega_i\omega_j D^S_{ij}/\langle \omega_i\omega_j S^*_{ij}\rangle$ for different cases are positive in both the compression and expansion regions. Their variations are similar to those of $\omega^2/\langle\omega^2\rangle$ and $D^S_{ij}D^S_{ij}/\langle D^S_{ij}D^S_{ij}\rangle$ (figure 3*a*,*b*). Furthermore, the magnitudes of $\omega_i\omega_j D^S_{ij}/\langle \omega_i\omega_j S^*_{ij}\rangle$ are comparable to those of $\omega_i\omega_j S^*_{ij}/\langle \omega_i\omega_j S^*_{ij}\rangle$, which agrees with the observations in table 7. For $\omega_i\omega_j D^D_{ij}/\langle \omega_i\omega_j S^*_{ij}\rangle$ and $-(1/6)\theta\omega^2/\langle \omega_i\omega_j S^*_{ij}\rangle$, their magnitudes are much smaller than those of $\omega_i\omega_j S^*_{ij}/\langle \omega_i\omega_j S^*_{ij}\rangle$. The magnitudes of $\omega_i\omega_j D^D_{ij}/\langle \omega_i\omega_j S^*_{ij}\rangle$ for different cases roughly equal 0.0 in the range of $-2.0 \leq \theta/\theta' \leq 2.0$. Beyond this range, the magnitudes of $\omega_i\omega_j D^D_{ij}/\langle \omega_i\omega_j S^*_{ij}\rangle$ increase with the local dilatation in both compression and expansion regions, and their growth rates are enhanced as the relaxation effect increases (figure 5*c*). The conditional averages of $-(1/6)\theta\omega^2/\langle \omega_i\omega_j S^*_{ij}\rangle$ for different cases are positive in the compression region, and negative in the expansion region; their magnitudes increase with the local dilatation (figure 5*d*). Interestingly, their growth rates are weakened as the relaxation effect increases, different from the $\omega_i\omega_j D^D_{ij}/\langle \omega_i\omega_j S^*_{ij}\rangle$ term.

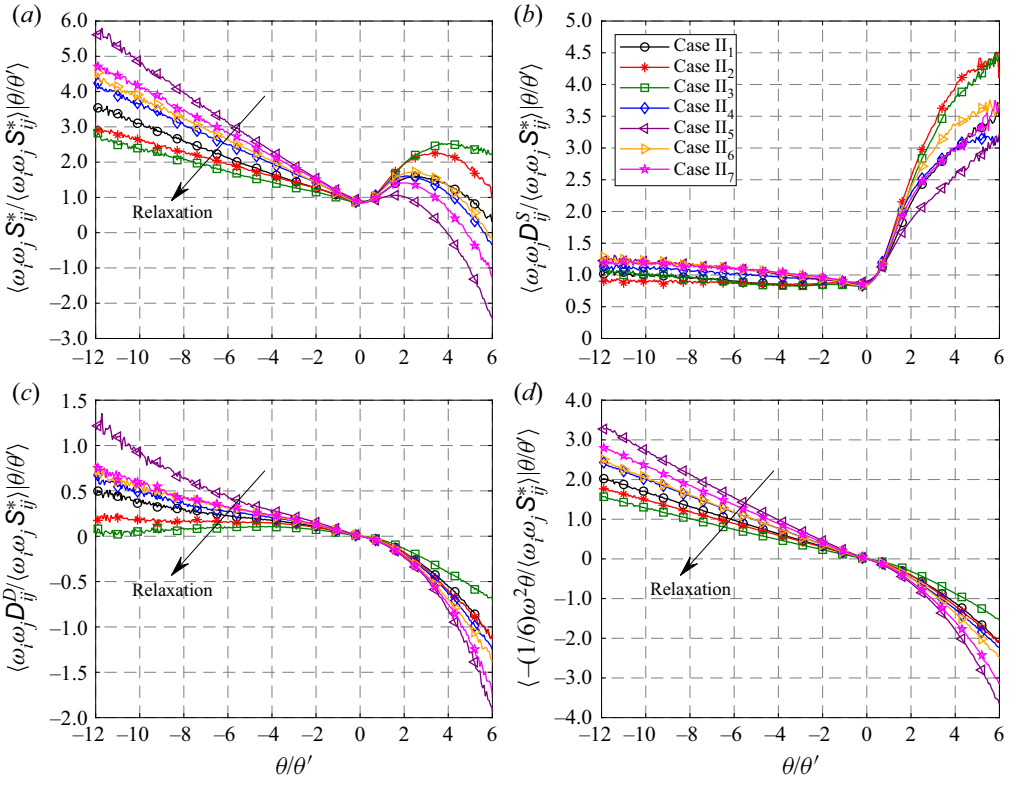

Figure 6. Conditional averages of the net enstrophy production and its components; (*a*) $\langle \omega_i\omega_j S^*_{ij}/\langle \omega_i\omega_j S^*_{ij}\rangle \mid \theta/\theta'\rangle$, (*b*) $\langle \omega_i\omega_j D^S_{ij}/\langle \omega_i\omega_j S^*_{ij}\rangle \mid \theta/\theta'\rangle$, (*c*) $\langle \omega_i\omega_j D^D_{ij}/\langle \omega_i\omega_j S^*_{ij}\rangle \mid \theta/\theta'\rangle$ and (*d*) $\langle -(1/6)\omega^2\theta/\langle \omega_i\omega_j S^*_{ij}\rangle \mid \theta/\theta'\rangle$. Here, $M_t \approx 0.68$.

For the $M_t \approx 0.68$ cases (figure 6), the conditional averages of net enstrophy production and its components are closely related to the local dilatation and vibrational relaxation. The conditional averages of $\omega_i\omega_j S^*_{ij}/\langle \omega_i\omega_j S^*_{ij}\rangle$ for different cases almost increase linearly with the local dilatation in the compression region, and their growth rates are weakened by the relaxation effect (figure 6*a*). In the expansion region, behaviours of $\omega_i\omega_j S^*_{ij}/\langle \omega_i\omega_j S^*_{ij}\rangle$ are rather complicated: they first increase with the local dilatation, then decrease from positive to negative. The weaker the relaxation effect, the sharper the decrease. This suggests that the compression enhances the enstrophy production; however, the high expansion weakens it. In the extreme expansion region (e.g. $\theta/\theta' > 4.0$ for case II$_5$), $\omega_i\omega_j S^*_{ij}$ can even become a enstrophy destruction term. As shown in figure 6(*b*), the conditional averages of $\omega_i\omega_j D^S_{ij}/\langle \omega_i\omega_j S^*_{ij}\rangle$ for different cases are nearly not affected by the local dilatation, remaining almost constant in the compression region. In the expansion region, the conditional averages of $\omega_i\omega_j D^S_{ij}/\langle \omega_i\omega_j S^*_{ij}\rangle$ are enlarged. Their differences among different cases are mainly manifested in the strong expansion region. Variations of $\omega_i\omega_j D^D_{ij}/\langle \omega_i\omega_j S^*_{ij}\rangle$ and $-(1/6)\theta\omega^2/\langle \omega_i\omega_j S^*_{ij}\rangle$ with the local dilatation are similar (figure 6*c*,*d*). They are positive in the compression region and negative in the expansion region, and their magnitudes increase with the local dilatation. Meanwhile, their growth rates are weakened by the relaxation effect in both compression and expansion regions.

However, the magnitude of $\omega_i\omega_j D_{ij}^D/\langle\omega_i\omega_j S_{ij}^*\rangle$ is smaller than that of $-(1/6)\theta\omega^2/\langle\omega_i\omega_j S_{ij}^*\rangle$ with the same dilatational level.

4.2. *Dilatational effect on deviatoric strain-rate tensor*

The interaction between strain and vorticity can be described in the eigenframe of the (deviatoric) strain-rate tensor. The modified strain-rate tensor is diagonalized into an orthonormal basis, with its eigenvalues given by λ_i for $i = 1, 2, 3$ (with $\lambda_1 \le \lambda_2 \le \lambda_3$) and the corresponding eigenvectors denoted by $\boldsymbol{\Lambda_i}$. Consequently, the net enstrophy production term can be rewritten as

$$\omega_i\omega_j S_{ij}^* = \omega^2[\lambda_1\cos^2(\omega, \Lambda_1) + \lambda_2\cos^2(\omega, \Lambda_2) + \lambda_3\cos^2(\omega, \Lambda_3)], \tag{4.4}$$

which isolates the individual contribution from each eigendirection. Similarly, the enstrophy production terms due to the solenoidal and dilatational components of the deviatoric strain-rate tensor ($\omega_i\omega_j D_{ij}^S$ and $\omega_i\omega_j D_{ij}^D$) can be rewritten as

$$\omega_i\omega_j D_{ij}^S = \omega^2[\lambda_1^S\cos^2(\omega, \Lambda_1^S) + \lambda_2^S\cos^2(\omega, \Lambda_2^S) + \lambda_3^S\cos^2(\omega, \Lambda_3^S)], \tag{4.5}$$

and

$$\omega_i\omega_j D_{ij}^D = \omega^2[\lambda_1^D\cos^2(\omega, \Lambda_1^D) + \lambda_2^D\cos^2(\omega, \Lambda_2^D) + \lambda_3^D\cos^2(\omega, \Lambda_3^D)]. \tag{4.6}$$

Here, λ_i^S (or λ_i^D) and Λ_i^S (or Λ_i^D) are the eigenvalues and eigenvectors of the solenoidal (or dilatational) component of the deviatoric strain-rate tensor ($\boldsymbol{D}$).

The first eigenvalue and the third eigenvalue always make a negative and a positive contribution to the enstrophy production, respectively, while the contribution of the second eigenvalue relies on its sign and magnitude. In addition, the orientation of the vorticity relative to the strain-rate eigenvector also plays a significant role in the enstrophy production. In the following discussions, effects of the vibrational relaxation and local dilatation on the statistical properties of strain-rate eigenvalues, alignments between the vorticity and strain-rate eigenvectors and individual contributions to enstrophy production from each eigendirection will be examined step by step.

In tables 9–12, the spatial averages of the eigenvalues, alignments between the vorticity and strain eigenvectors and the individual contributions to the enstrophy production in each eigendirection are summarized. The variable β_i^X (X denotes D or S) is defined as

$$\beta_i^X = \frac{\lambda_i^X}{\sqrt{(\lambda_1^X)^2 + (\lambda_2^X)^2 + (\lambda_3^X)^2}}, \tag{4.7}$$

which represents the relative amplitude of λ_i^X. For the solenoidal component of the deviatoric strain-rate tensor (tables 9 and 11), the vibrational relaxation has little influence on the ratio of $\langle\beta_i^S\rangle$. The ratio of $\langle\beta_i^S\rangle$ is approximately $-0.743{:}0.117{:}0.626$ for both the $M_t \approx 0.22$ and 0.68 cases. The ratio of $\langle\mathrm{Cos}^2(\omega, \Lambda_i^S)\rangle$ roughly equals $0.158{:}0.528{:}0.314$ for the $M_t \approx 0.22$ cases, and $0.155{:}0.542{:}0.303$ for the $M_t \approx 0.68$ cases. The alignment between the vorticity and the third eigenvector is enhanced slightly for the $M_t \approx 0.22$ cases, such that the dominant contribution to $\omega_i\omega_j D_{ij}^S$ arises from the third eigendirection for the $M_t \approx 0.22$ cases, while it results from the second eigendirection for the $M_t \approx 0.68$ cases (tables 9 and 11). The ratio of $\langle\omega^2\lambda_i^S\mathrm{Cos}^2(\omega, \Lambda_i^S)/\langle\omega_i\omega_j S_{ij}^*\rangle\rangle$ roughly equals $-0.348{:}0.632{:}0.716$ and $-0.285{:}0.672{:}0.619$ for the $M_t \approx 0.22$ and 0.68

Case	$\langle\beta_i^S\rangle$	$\langle\mathrm{Cos}^2(\omega, \Lambda_i^S)\rangle$	$\langle\omega^2\lambda_i^S\mathrm{Cos}^2(\omega, \Lambda_i^S)/\langle\omega_i\omega_j\mathcal{S}_{ij}^*\rangle\rangle$
I_1	−0.743 : 0.118 : 0.625	0.158 : 0.528 : 0.314	−0.350 : 0.632 : 0.720
I_2	−0.743 : 0.118 : 0.625	0.157 : 0.530 : 0.313	−0.346 : 0.633 : 0.714
I_3	−0.743 : 0.118 : 0.625	0.158 : 0.527 : 0.315	−0.351 : 0.632 : 0.721
I_4	−0.743 : 0.118 : 0.625	0.157 : 0.528 : 0.315	−0.346 : 0.633 : 0.713
I_5	−0.743 : 0.118 : 0.625	0.157 : 0.530 : 0.313	−0.343 : 0.634 : 0.707
I_6	−0.743 : 0.118 : 0.625	0.158 : 0.527 : 0.315	−0.350 : 0.630 : 0.721
I_7	−0.743 : 0.118 : 0.625	0.158 : 0.528 : 0.314	−0.350 : 0.633 : 0.717

Table 9. Statistics of various quantities in three eigendirections about $\omega_i\omega_j D_{ij}^S$. Here, $M_t \approx 0.22$.

Case	$\langle\beta_i^D\rangle$	$\langle\mathrm{Cos}^2(\omega, \Lambda_i^D)\rangle$	$\langle\omega^2\lambda_i^D\mathrm{Cos}^2(\omega, \Lambda_i^D)/\langle\omega_i\omega_j\mathcal{S}_{ij}^*\rangle\rangle$
I_1	−0.702 : 0.030 : 0.672	0.325 : 0.348 : 0.328	−0.056 : 0.003 : 0.052
I_2	−0.696 : 0.019 : 0.677	0.322 : 0.356 : 0.322	−0.035 : 0.002 : 0.034
I_3	−0.696 : 0.019 : 0.678	0.323 : 0.354 : 0.324	−0.036 : 0.001 : 0.033
I_4	−0.701 : 0.027 : 0.674	0.328 : 0.342 : 0.330	−0.100 : 0.006 : 0.094
I_5	−0.705 : 0.036 : 0.669	0.328 : 0.342 : 0.329	−0.224 : 0.022 : 0.204
I_6	−0.701 : 0.028 : 0.673	0.326 : 0.346 : 0.328	−0.062 : 0.004 : 0.057
I_7	−0.705 : 0.034 : 0.670	0.327 : 0.343 : 0.330	−0.104 : 0.008 : 0.096

Table 10. Statistics of various quantities in three eigendirections about $\omega_i\omega_j D_{ij}^D$. Here, $M_t \approx 0.22$.

Case	$\langle\beta_i^S\rangle$	$\langle\mathrm{Cos}^2(\omega, \Lambda_i^S)\rangle$	$\langle\omega^2\lambda_i^S\mathrm{Cos}^2(\omega, \Lambda_i^S)/\langle\omega_i\omega_j\mathcal{S}_{ij}^*\rangle\rangle$
II_1	−0.742 : 0.116 : 0.627	0.155 : 0.543 : 0.302	−0.280 : 0.675 : 0.612
II_2	−0.742 : 0.115 : 0.627	0.155 : 0.542 : 0.302	−0.284 : 0.675 : 0.615
II_3	−0.742 : 0.116 : 0.626	0.155 : 0.542 : 0.303	−0.285 : 0.668 : 0.624
II_4	−0.742 : 0.116 : 0.626	0.155 : 0.542 : 0.303	−0.284 : 0.674 : 0.618
II_5	−0.742 : 0.116 : 0.627	0.156 : 0.541 : 0.303	−0.287 : 0.669 : 0.621
II_6	−0.742 : 0.116 : 0.627	0.155 : 0.541 : 0.304	−0.286 : 0.671 : 0.621
II_7	−0.742 : 0.116 : 0.627	0.155 : 0.541 : 0.304	−0.288 : 0.673 : 0.622

Table 11. Statistics of various quantities in three eigendirections about $\omega_i\omega_j D_{ij}^S$. Here, $M_t \approx 0.68$.

cases, respectively. Here, the sum of $\langle\omega^2\lambda_i^S\mathrm{Cos}^2(\omega, \Lambda_i^S)/\langle\omega_i\omega_j\mathcal{S}_{ij}^*\rangle\rangle$ for each case is approximately 1.0, implying that the net enstrophy production mainly stems from the solenoidal component of the deviatoric strain-rate tensor from the full flow field perspective. This observation agrees with the results in table 7.

Values of $\langle\beta_i^D\rangle$, $\langle\mathrm{Cos}^2(\omega, \Lambda_i^D)\rangle$ and $\langle\omega^2\lambda_i^D\mathrm{Cos}^2(\omega, \Lambda_i^D)/\langle\omega_i\omega_j\mathcal{S}_{ij}^*\rangle\rangle$ (tables 10 and 12) are very different from those for the solenoidal component of the deviatoric strain-rate tensor. The magnitudes of $\langle\beta_1^D\rangle$ and $\langle\beta_3^D\rangle$ are close to each other, while that of $\langle\beta_2^D\rangle$ is much smaller. In addition, $\langle\beta_2^D\rangle$ and $\langle\beta_3^D\rangle$ are positive, and $\langle\beta_1^D\rangle + \langle\beta_2^D\rangle + \langle\beta_3^D\rangle = 0.0$. The ratio of $\langle\mathrm{Cos}^2(\omega, \Lambda_i^D)\rangle$ approximately equals 0.326:0.347:0.327 for the $M_t \approx 0.22$ cases, and 0.318:0.370:0.311 for the $M_t \approx 0.68$ cases. The value of $\langle\mathrm{Cos}^2(\omega, \Lambda_i^D)\rangle$ roughly approaches 1/3 for each eigenvector, implying that ω and Λ_i^D are nearly distributed independently and uniformly from the full flow field perspective.

Case	$\langle\beta_i^D\rangle$	$\langle\mathrm{Cos}^2(\omega, \Lambda_i^D)\rangle$	$\langle\omega^2\lambda_i^D\mathrm{Cos}^2(\omega, \Lambda_i^D)/\langle\omega_i\omega_j S_{ij}^*\rangle\rangle$
II_1	−0.700 : 0.024 : 0.675	0.317 : 0.372 : 0.310	−0.128 : 0.009 : 0.116
II_2	−0.699 : 0.022 : 0.676	0.318 : 0.370 : 0.312	−0.109 : 0.007 : 0.100
II_3	−0.697 : 0.018 : 0.679	0.319 : 0.369 : 0.312	−0.093 : 0.004 : 0.086
II_4	−0.698 : 0.020 : 0.677	0.320 : 0.371 : 0.309	−0.128 : 0.009 : 0.116
II_5	−0.702 : 0.031 : 0.671	0.317 : 0.371 : 0.312	−0.175 : 0.017 : 0.158
II_6	−0.700 : 0.024 : 0.675	0.318 : 0.371 : 0.312	−0.130 : 0.010 : 0.118
II_7	−0.701 : 0.027 : 0.673	0.318 : 0.370 : 0.311	−0.152 : 0.013 : 0.137

Table 12. Statistics of various quantities in three eigendirections about $\omega_i\omega_j D_{ij}^D$. Here, $M_t \approx 0.68$.

The sum of $\langle\omega^2\lambda_i^D\mathrm{Cos}^2(\omega, \Lambda_i^D)/\langle\omega_i\omega_j S_{ij}^*\rangle\rangle$ for each case is approximately 0.0, indicating the negligible contribution from the dilatational component of the deviatoric strain-rate tensor to the net enstrophy production. The magnitudes of $\langle\omega^2\lambda_1^D\mathrm{Cos}^2(\omega, \Lambda_1^D)/\langle\omega_i\omega_j S_{ij}^*\rangle\rangle$ and $\langle\omega^2\lambda_3^D\mathrm{Cos}^2(\omega, \Lambda_3^D)/\langle\omega_i\omega_j S_{ij}^*\rangle\rangle$ are comparable, while that of $\langle\omega^2\lambda_2^D\mathrm{Cos}^2(\omega, \Lambda_2^D)/\langle\omega_i\omega_j S_{ij}^*\rangle\rangle$ is one order of magnitude smaller than the other two components. This should be attributed to the smaller $\langle\beta_2^D\rangle$. Meanwhile, the magnitude of $\langle\omega^2\lambda_i^D\mathrm{Cos}^2(\omega, \Lambda_i^D)/\langle\omega_i\omega_j S_{ij}^*\rangle\rangle$ is enlarged as the relaxation effect fades. For instance, the ratios of $\langle\omega^2\lambda_i^D\mathrm{Cos}^2(\omega, \Lambda_i^D)/\langle\omega_i\omega_j S_{ij}^*\rangle\rangle$ are respectively approximately −0.036:0.001:0.033 and −0.224:0.022:0.204 for cases I_3 and I_5 (table 10).

Figure 7 shows the PDFs and conditional PDFs of the normalized eigenvalues of D_{ij}^S for cases I_3 and I_5, and figure 8 for cases II_3 and II_5. The three normalized eigenvalues of D_{ij}^S are respectively located in the ranges of $[-0.816, -0.408]$, $[-0.408, 0.408]$ and $[0.408, 0.816]$. For cases I_3 and II_3, where the relaxation effect is significant, the lines corresponding to different dilatational levels have a slight deviation; however, their peaks are close (figures 7(*a*), 8(*a*)). When the relaxation effect declines (e.g. cases I_5 and II_5), the lines corresponding to different dilatational levels almost overlap each other (figures 7(*b*), 8(*b*)). The effects of local dilatation and vibrational relaxation on the PDF of β_i^S are negligible, and this is consistent with the observations in tables 9 and 11. In the overall flow field, the preferred eigenvalue ratio is approximately −4.0:1.0:3.0, in good agreement with the results in incompressible turbulent flows (Ashurst *et al.* 1987).

Figures 9 and 10 present the PDFs and conditional PDFs of the normalized eigenvalues of D_{ij}^D for cases I_3 and I_5, as well as cases II_3 and II_5, respectively. Although the conditional PDFs of β_i^D are closely related to the local dilatational and vibrational relaxation, the preferred ratio of β_i^D is approximately −0.81:0.1:0.80 in the overall flow field for both the $M_t \approx 0.22$ and 0.68 cases. The first eigenvalue with $\beta_1^D \approx -0.81$ dominates in compression regions, while the third eigenvalue with $\beta_3^D \approx 0.80$ dominates in expansion regions (figures 9(*a*,*c*,*d*,*f*) and 10(*a*,*c*,*d*,*f*)). When the flow compressibility is weak (e.g. case I_3), the peak value of the conditional PDF of β_1^D in the compression region is much smaller than the other cases. Furthermore, the conditional PDFs of β_1^D do not have an obvious peak in the expansion region. The intermediate eigenvalue β_2^D tends to be positive in the compression region, and negative in the expansion region. As the flow compressibility increases, this tendency becomes obvious (figures 9(*b*,*e*) and 10(*b*,*e*)). The third eigenvalue β_3^D is positive. The value of β_3^D in the compression region becomes smaller with the increase of flow compressibility, while that in the expansion region almost

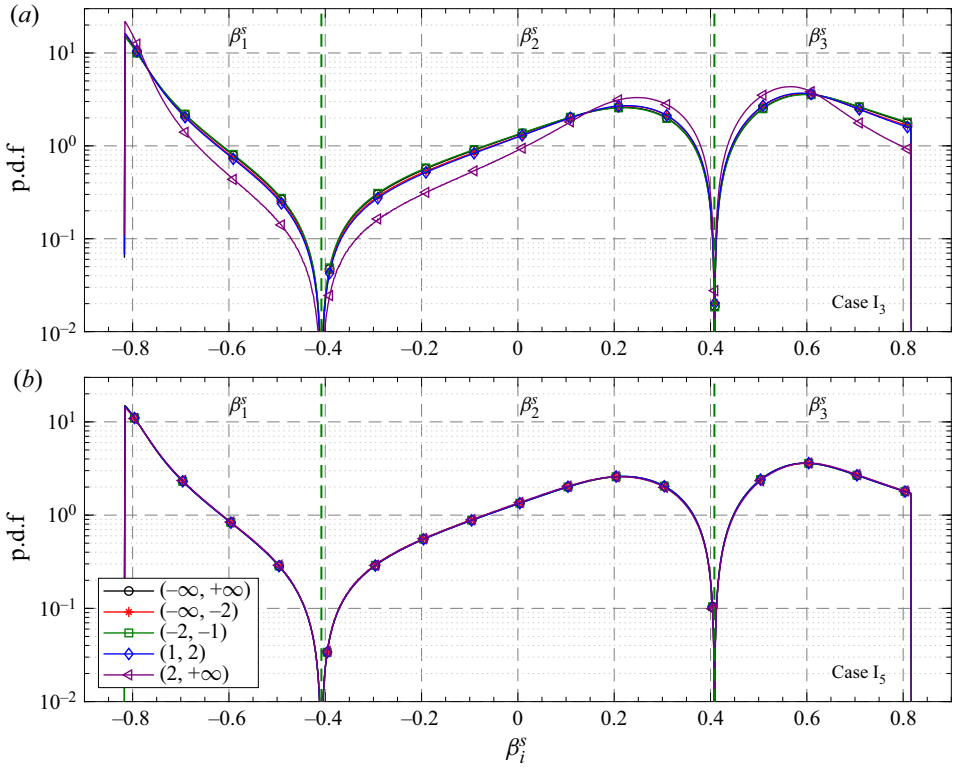

Figure 7. The PDFs and conditional PDFs of the normalized eigenvalues of D_{ij}^S. (*a*) Case I_3 and (*b*) case I_5.

does not change. For instance, the preferred β_2^D and β_3^D in the strong compression region approximately equal 0.11 and 0.79, respectively, for case I_3; these values roughly equal 0.34 and 0.47, respectively, for case I_5. The values of β_2^D and β_3^D become close in the strong compression region as the flow compressibility increases, which implies that the highly compressible structures are primarily sheet like, and parallel to the plane formed by Λ_2^D and Λ_3^D.

Figures 11 and 12 display the PDFs and conditional PDFs of the alignments between the vorticity and eigenvectors of the deviatoric strain-rate components (D_{ij}^D and D_{ij}^S) for cases I_3 and I_5, respectively. The alignments between the vorticity and eigenvectors of D_{ij}^S are almost identical to those for incompressible turbulence (Ashurst *et al.* 1987; Buaria *et al.* 2020) and weakly compressible turbulence (Pirozzoli & Grasso 2004; Lee *et al.* 2009). There is a strong tendency for the vorticity to be perpendicular to the first eigenvector and align with the intermediate eigenvector (figures 11(*a*,*b*) and 12(*a*,*b*)). The PDF and conditional PDFs of $\cos(\omega, \Lambda_3^S)$ approximately equal 0.5, implying that the distribution of angle between the vorticity and the third eigenvector is relatively uniform (figures 11(*c*), 12(*c*)). Similar observations are made for the $M_t \approx 0.68$ cases (not shown). Thus, the effects of the vibrational relaxation and dilatation on the alignments between the vorticity and eigenvectors of D_{ij}^S are negligible. The above observations agree well with the results of tables 5 and 6, where $\mathrm{Corr}(\omega^2, D_{ij}^S D_{ij}^S)$ is found to be independent of the vibrational relaxation.

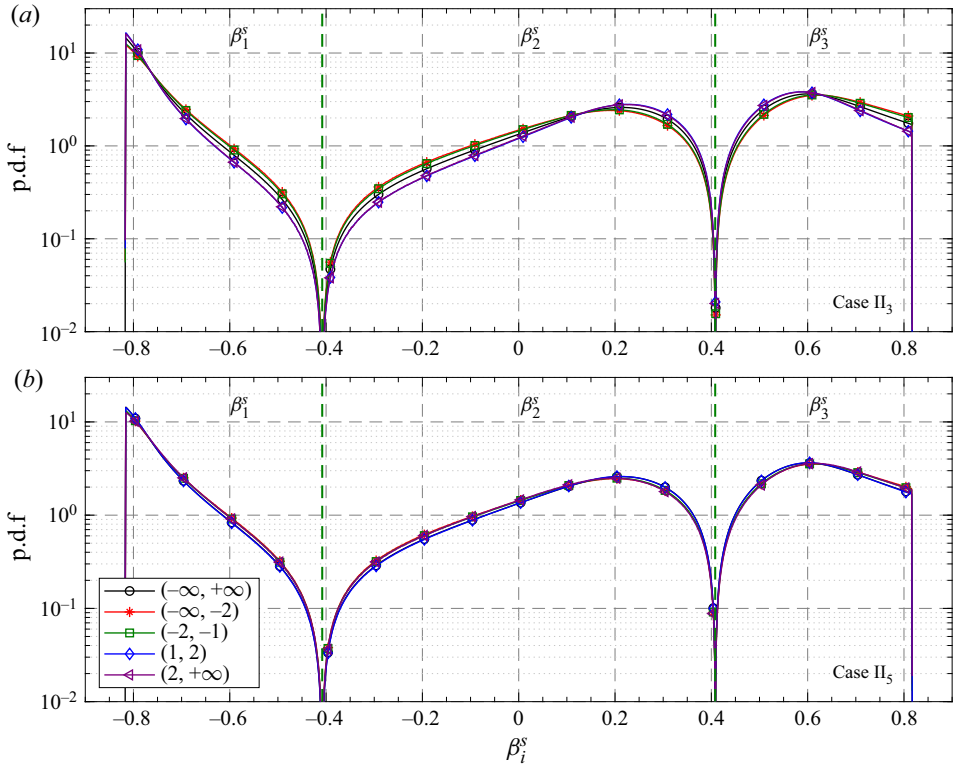

Figure 8. The PDFs and conditional PDFs of the normalized eigenvalues of D_{ij}^S. (*a*) Case II$_3$ and (*b*) case II$_5$.

Obviously, alignments between the vorticity and eigenvectors of D_{ij}^D are closely related to the vibrational relaxation and local dilatation. For case I$_3$, there is a tendency for the vorticity to be perpendicular to the first eigenvector in the strong compressible region, and to strongly align with the first eigenvector in the strong expansion region (figure 11*d*). Note that the tendency is weakened as the local dilatation decreases. As shown in figure 11(*e*), the vorticity slightly aligns with the intermediate eigenvector only in the strong expansion region. Contrary to the first eigenvector, the vorticity tends to align with the third eigenvector in the strong compressible region, and to be strongly perpendicular to the third eigenvector in the strong expansion region (figure 11*f*). However, for case I$_5$, where the relaxation effect is weak, there is no obvious tendency for alignment between the vorticity and eigenvectors of D_{ij}^D. The PDF and conditional PDFs of $\cos(\omega, \Lambda_i^D)$ approximately equal 0.5 (figure 12*d*,*e*,*f*).

Figure 13 displays the PDFs and conditional PDFs of the alignments between the vorticity and eigenvectors of D_{ij}^D for cases II$_3$ and II$_5$. The conditional PDFs of $\cos(\omega, \Lambda_i^D)$ are similar for cases II$_3$ and II$_5$. The vorticity aligns with the first eigenvector in the expansion region, and with the third eigenvector in the compression region. Meanwhile, the vorticity tends to be perpendicular to the first eigenvector in the compression region, and to the third eigenvector in the expansion region. The alignment between the vorticity and the second eigenvector of D_{ij}^D is not clear for both cases II$_3$ and II$_5$ (figure 13*b*,*e*). These observations are similar to that for case I$_3$. This suggests that alignments between the vorticity and eigenvectors of D_{ij}^D are closely related to the flow compressibility for both

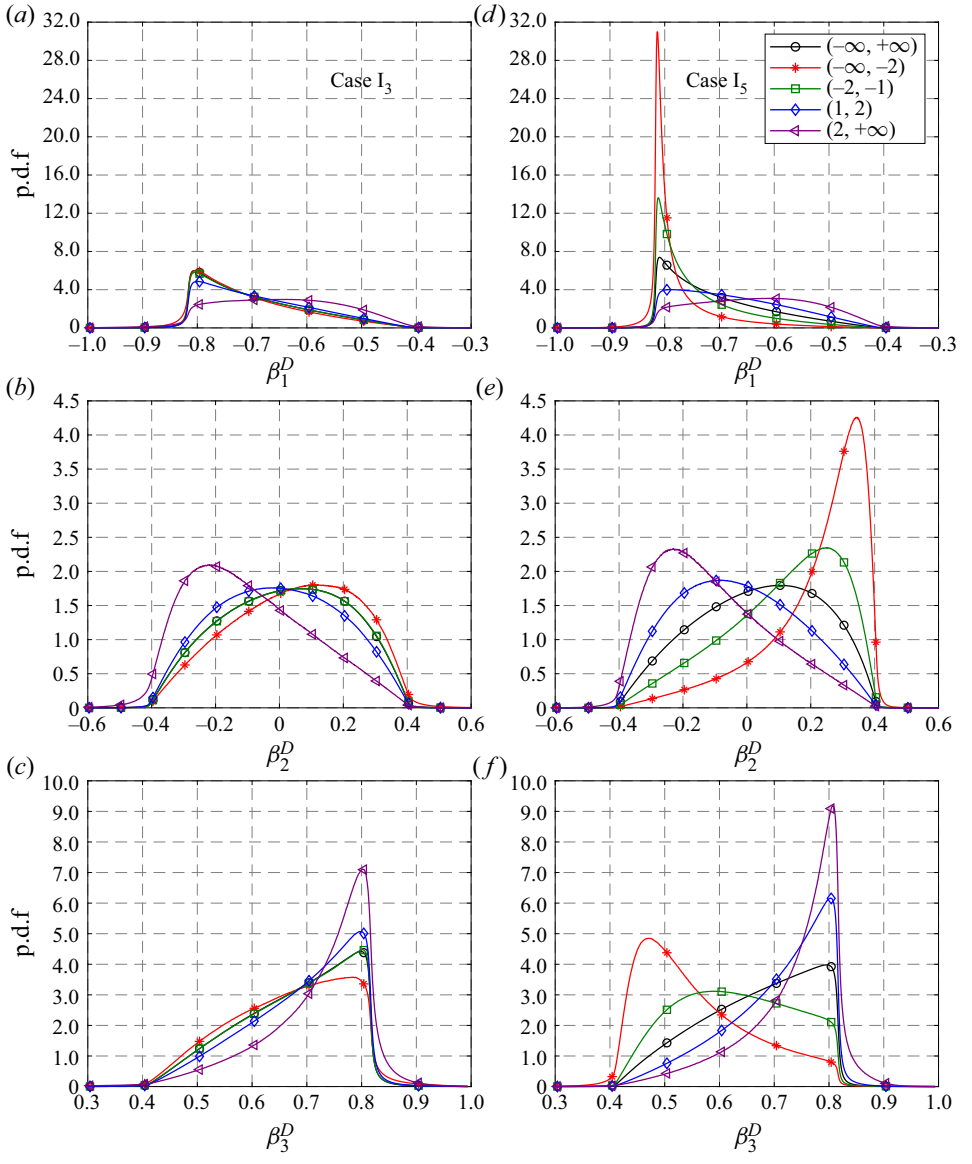

Figure 9. The PDFs and conditional PDFs of the normalized eigenvalues of D_{ij}^D. (*a–c*) Case I_3 and (*d–f*) case I_5.

the $M_t \approx 0.22$ and 0.68 cases. The stronger the flow compressibility, the less significant the alignments between the vorticity and eigenvectors of D_{ij}^D.

Figures 14 and 15 display the conditional averages of the enstrophy production along the three eigendirections of D_{ij}^S and D_{ij}^D for the $M_t \approx 0.22$ and 0.68 cases, respectively. As shown in figure 14(*a*,*b*,*c*), the conditional averages of $\omega^2\lambda_1^S\cos^2(\omega, \Lambda_1^S)/\langle\omega_i\omega_j S_{ij}^*\rangle$ are negative, while those of $\omega^2\lambda_2^S\cos^2(\omega, \Lambda_2^S)/\langle\omega_i\omega_j S_{ij}^*\rangle$ and $\omega^2\lambda_3^S\cos^2(\omega, \Lambda_3^S)/\langle\omega_i\omega_j S_{ij}^*\rangle$ are positive in both compression and expansion regions. The ratio of the conditional averages of $\omega^2\lambda_i^S\cos^2(\omega, \Lambda_i^S)/\langle\omega_i\omega_j S_{ij}^*\rangle$ is close to −0.33:0.58:0.66 at $\theta/\theta' = 0.0$. The magnitude

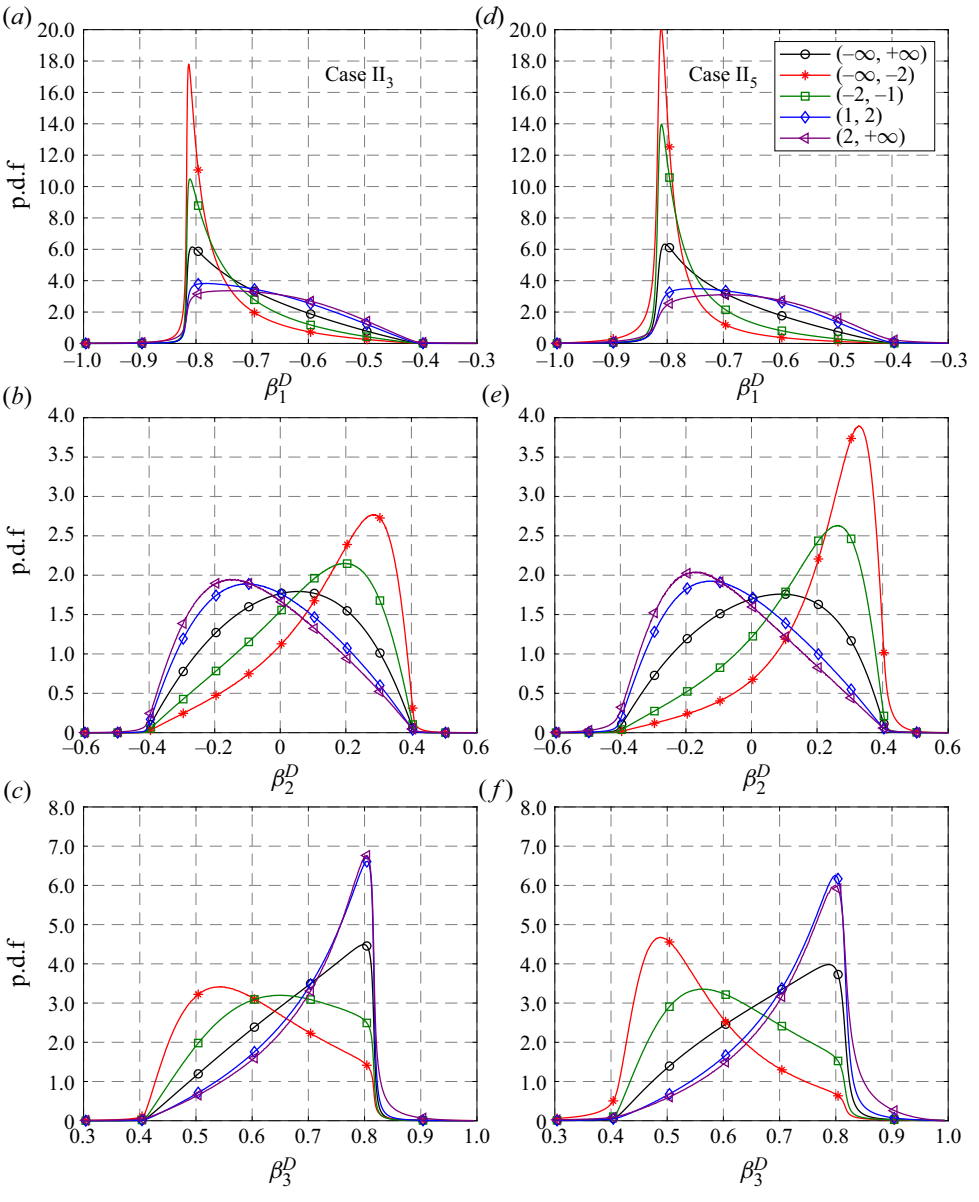

Figure 10. The PDFs and conditional PDFs of the normalized eigenvalues of D_{ij}^D. (*a–c*) Case II_3 and (*d–f*) case II_5.

of the conditional average of $\omega^2\lambda_1^S\cos^2(\omega, \Lambda_1^S)/\langle\omega_i\omega_j S_{ij}^*\rangle$ for each case is much smaller than those of the other two components. Furthermore, as mentioned above, the PDFs and conditional PDFs of β_i^S and $\cos(\omega, \Lambda_i^S)$ are nearly independent of the local dilatation and vibrational relaxation. Therefore, the variations of $\omega^2\lambda_i^S\cos^2(\omega, \Lambda_i^S)/\langle\omega_i\omega_j S_{ij}^*\rangle$ are thus mainly affected by the vorticity. Here, we can observe that the dependencies of magnitudes of $\omega^2\lambda_i^S\cos^2(\omega, \Lambda_i^S)/\langle\omega_i\omega_j S_{ij}^*\rangle$ on the local dilatation are similar to those of $\omega^2/\langle\omega^2\rangle$ (figure 3*a*).

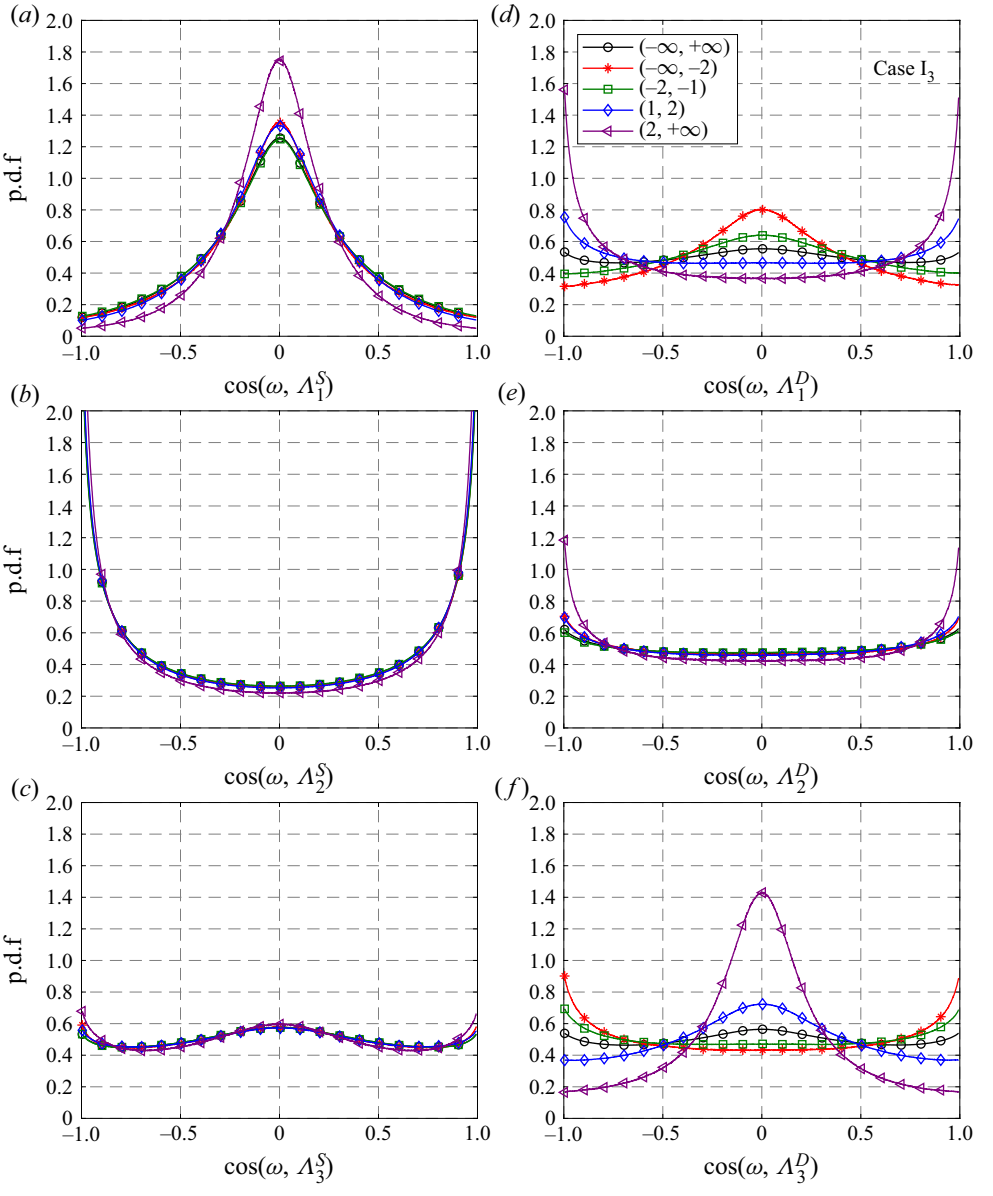

Figure 11. The PDFs and conditional PDFs of the alignments between the vorticity and the eigenvectors (*a–c*) Λ_i^S and (*d–f*) Λ_i^D. Case I_3.

Along the eigendirections of D_{ij}^D, the conditional averages of $\omega^2\lambda_1^D\cos^2(\omega, \Lambda_1^D)/\langle\omega_i\omega_j S_{ij}^*\rangle$ and $\omega^2\lambda_3^D\cos^2(\omega, \Lambda_3^D)/\langle\omega_i\omega_j S_{ij}^*\rangle$ are negative and positive, respectively; while those of $\omega^2\lambda_2^D\cos^2(\omega, \Lambda_2^D)/\langle\omega_i\omega_j S_{ij}^*\rangle$ are positive in the compression region and negative in the expansion region (figure 14*d*,*e*,*f*). Their magnitudes are enlarged with the increase of dilatation, and their growth rates are weakened by the relaxation effect. When the relaxation effect is significant (e.g. case I_3), the magnitudes of conditional averages of $\omega^2\lambda_1^D\cos^2(\omega, \Lambda_1^D)/\langle\omega_i\omega_j S_{ij}^*\rangle$ in the compression region and $\omega^2\lambda_3^D\cos^2(\omega, \Lambda_3^D)/\langle\omega_i\omega_j S_{ij}^*\rangle$

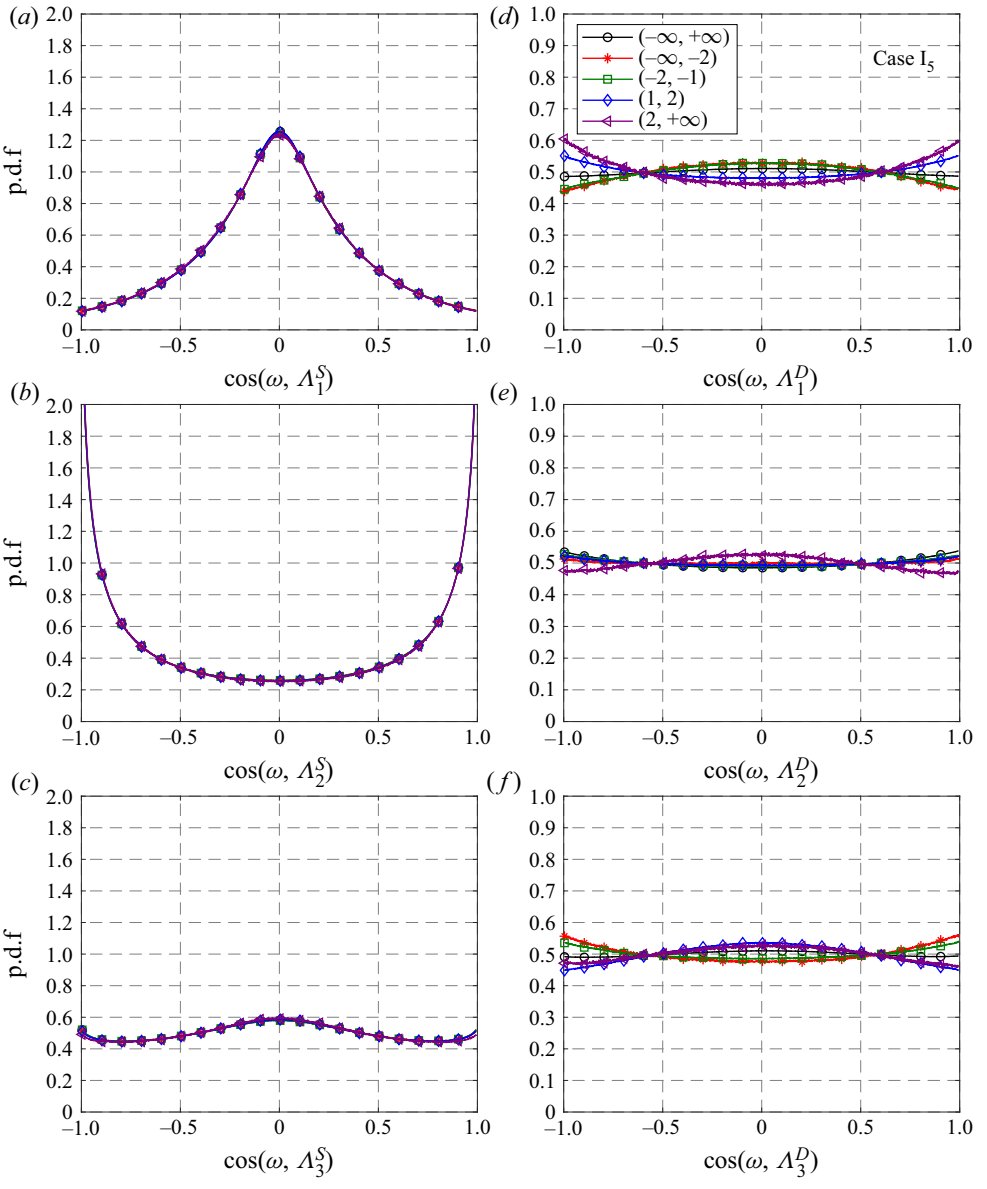

Figure 12. The PDFs and conditional PDFs of alignments between the vorticity and the eigenvectors (*a–c*) Λ_i^S and (*d–f*) Λ_i^D. Case I_5.

in the expansion region are close to zero and almost remain constant. This is due to the fact that the conditional average of $\cos(\omega, \Lambda_1^D)$ in the compression region and that of $\cos(\omega, \Lambda_3^D)$ in the expansion region tend to be zero (figure 11*d*,*f*). The above observations suggest that, different from $\omega^2\lambda_i^S\cos^2(\omega, \Lambda_i^S)/\langle\omega_i\omega_j S_{ij}^*\rangle$, the dependency of $\omega^2\lambda_i^D\cos^2(\omega, \Lambda_i^D)/\langle\omega_i\omega_j S_{ij}^*\rangle$ on the local dilatation is affected by the vorticity, eigenvalues and alignments between the vorticity and strain eigenvectors.

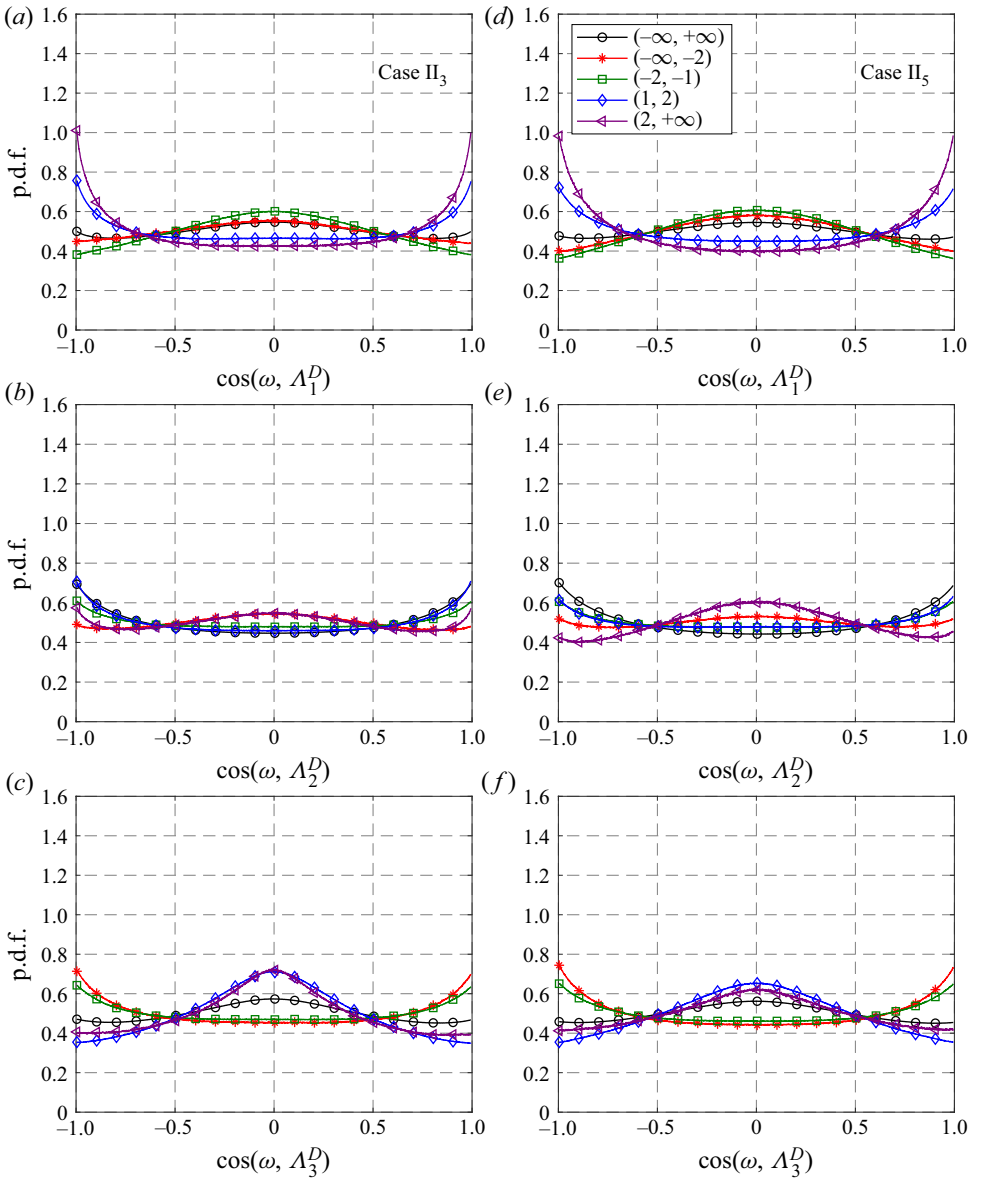

Figure 13. The PDFs and conditional PDFs of alignments between the vorticity and the eigenvector Λ_i^D. (a–c) Case II$_3$ and (d–f) case II$_5$.

For the $M_t \approx 0.68$ cases, as presented in figure 15(a,b,c), the conditional averages of $\omega^2\lambda_1^S\cos^2(\omega, \Lambda_1^S)/\langle\omega_i\omega_j S_{ij}^*\rangle$ are negative in both compression and expansion regions, while those of $\omega^2\lambda_2^S\cos^2(\omega, \Lambda_2^S)/\langle\omega_i\omega_j S_{ij}^*\rangle$ and $\omega^2\lambda_3^S\cos^2(\omega, \Lambda_3^S)/\langle\omega_i\omega_j S_{ij}^*\rangle$ are positive. The ratio of conditional averages of $\omega^2\lambda_i^S\cos^2(\omega, \Lambda_i^S)/\langle\omega_i\omega_j S_{ij}^*\rangle$ is close to $-0.25{:}0.57{:}0.54$ at $\theta/\theta' = 0.0$. Their magnitudes almost remain constant in the range of $\theta/\theta' < -4.0$, decline in the range of $-4.0 \le \theta/\theta' \le 0.0$ and increase sharply in the expansion region. The influence of vibrational relaxation is mainly manifested in the strong expansion region, especially for the intermediate eigendirection. It can be expected

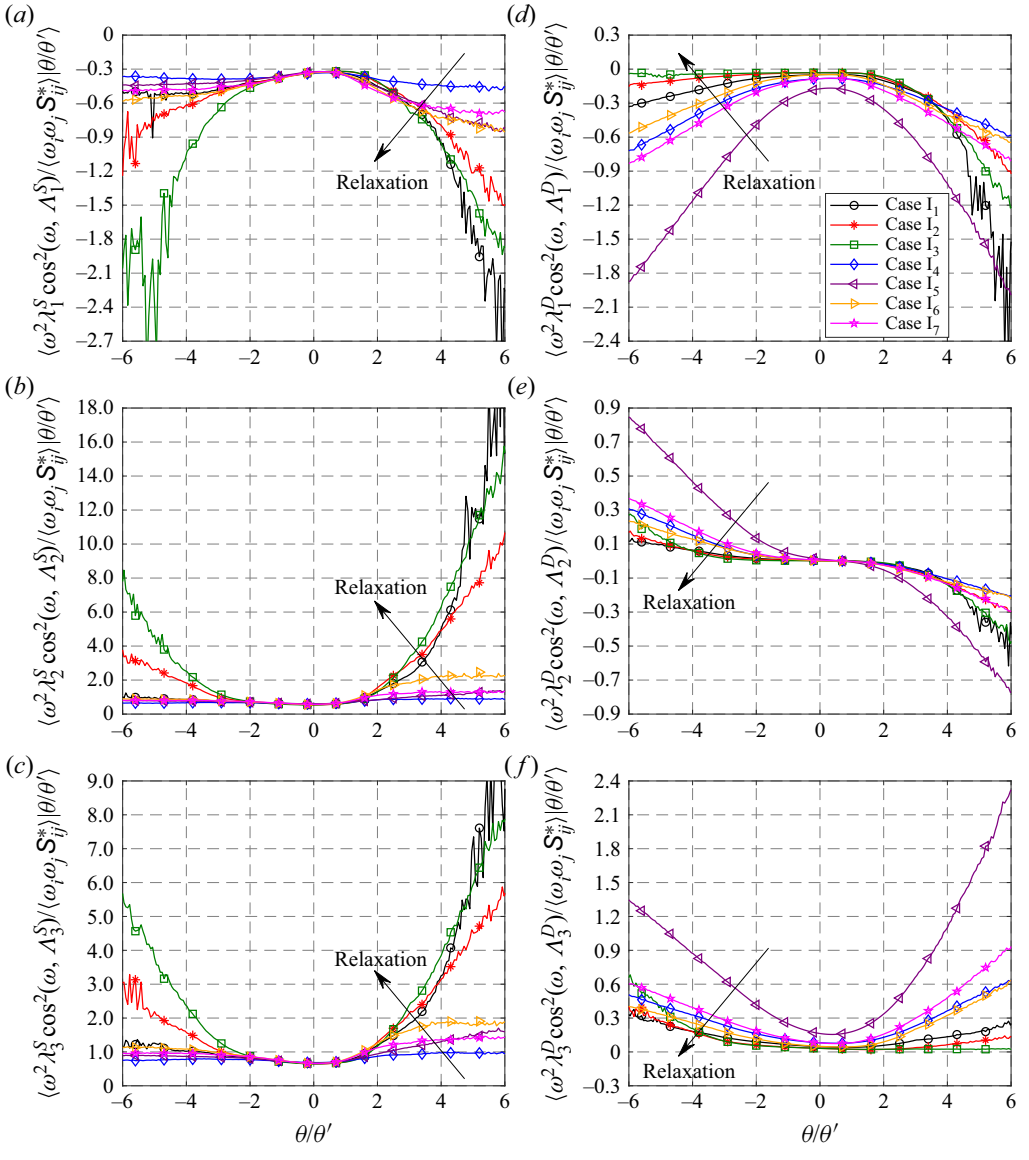

Figure 14. Conditional averages of the enstrophy production components along the three eigendirections of the deviatoric strain-rate components (*a–c*) D_{ij}^S and (*d–f*) D_{ij}^D. Here, $M_t \approx 0.22$.

that the conditional averages of $\omega^2\lambda_i^S\cos^2(\omega, \Lambda_i^S)/\langle\omega_i\omega_j S_{ij}^*\rangle$ mainly relate to the vorticity. Note that the magnitude of the conditional average of $\omega^2\lambda_1^S\cos^2(\omega, \Lambda_1^S)/\langle\omega_i\omega_j S_{ij}^*\rangle$ for each case is approximately half that of the other two components. On the other hand, the conditional averages of $\omega^2\lambda_1^D\cos^2(\omega, \Lambda_1^D)/\langle\omega_i\omega_j S_{ij}^*\rangle$ and $\omega^2\lambda_3^D\cos^2(\omega, \Lambda_3^D)/\langle\omega_i\omega_j S_{ij}^*\rangle$ are respectively negative and positive in both compression and expansion regions; while those of $\omega^2\lambda_2^D\cos^2(\omega, \Lambda_2^D)/\langle\omega_i\omega_j S_{ij}^*\rangle$ are positive in the compression region and negative in the expansion region (figure 15*d,e,f*). The magnitudes of conditional averages of $\omega^2\lambda_i^D\cos^2(\omega, \Lambda_i^D)/\langle\omega_i\omega_j S_{ij}^*\rangle$ along three eigendirections are close to zero at $\theta/\theta' = 0.0$.

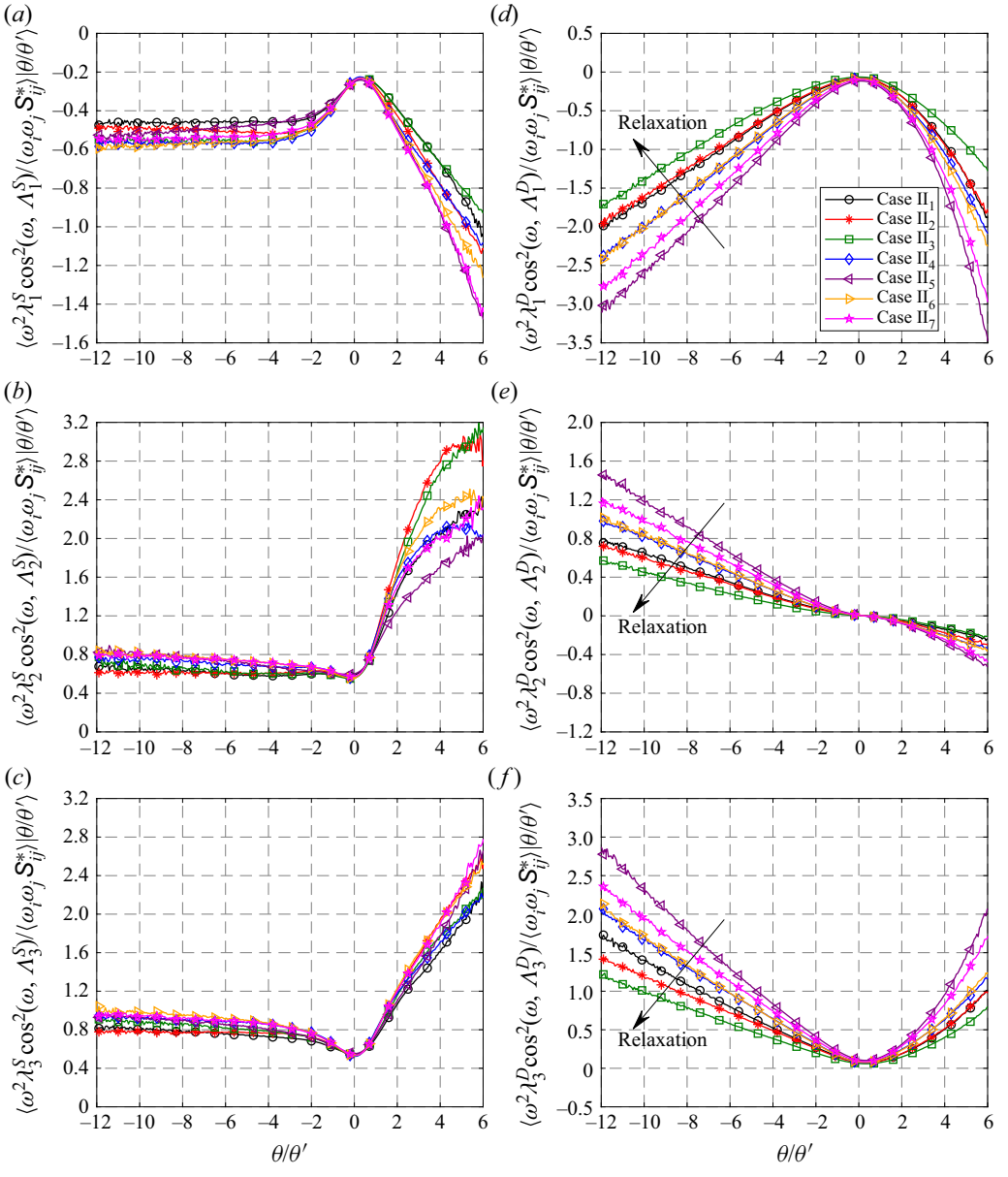

Figure 15. Conditional averages of enstrophy production components along the three eigendirections of the deviatoric strain-rate components (*a–c*) D_{ij}^S and (*d–f*) D_{ij}^D. Here, $M_t \approx 0.68$.

Their magnitudes are enlarged with the increase of dilatation, and their growth rates are weakened by the relaxation effect. Meanwhile, the magnitude of the conditional average of $\omega^2\lambda_1^D\cos^2(\omega, \Lambda_1^D)/\langle\omega_i\omega_j S_{ij}^*\rangle$ for each case is slightly larger than that of $\omega^2\lambda_3^D\cos^2(\omega, \Lambda_3^D)/\langle\omega_i\omega_j S_{ij}^*\rangle$, while that of $\omega^2\lambda_2^D\cos^2(\omega, \Lambda_2^D)/\langle\omega_i\omega_j S_{ij}^*\rangle$ is much smaller. The above observations are consistent with the results in tables 11 and 12.

5. Flow topology of compressible turbulence in non-equilibrium

Based on the topological classification proposed by Chong *et al.* (1990), the local flow pattern in a compressible flow field can be deduced by the three invariants of the velocity gradient tensor $\boldsymbol{A}$ ($A_{ij} = \partial u_j/\partial x_i$). The first, second and third invariants of A_{ij} are respectively denoted by P, Q and R, which are defined as

$$P = -(\xi_1 + \xi_2 + \xi_3) = -\theta, \tag{5.1}$$

$$Q = \xi_1\xi_2 + \xi_2\xi_3 + \xi_3\xi_1 = (P^2 - S_{ij}S_{ij} + R_{ij}R_{ij})/2, \tag{5.2}$$

and

$$R = -\xi_1\xi_2\xi_3 = (-P^3 + 3PQ - S_{ij}S_{jk}S_{ki} - 3R_{ij}R_{jk}S_{ki})/3. \tag{5.3}$$

Here, $R_{ij} = (\partial u_i/\partial x_j - \partial u_j/\partial x_i)/2$ is the component of the skew–symmetric rotation tensor. The three eigenvalues of the velocity gradient tensor are denoted as ξ_i ($i = 1, 2, 3$), which satisfy the following characteristic equation:

$$\xi_i^3 + P\xi_i^2 + Q\xi_i + R = 0. \tag{5.4}$$

The discriminant Δ of the velocity gradient tensor is given as

$$\Delta = 27R^2 + (4P^3 - 18PQ)R + (4Q^3 - P^2Q^2). \tag{5.5}$$

If $\Delta < 0$, the three eigenvalues of the velocity gradient tensor are all real: $\xi_1 \leq \xi_2 \leq \xi_3$. If $\Delta > 0$, only one eigenvalue is real, and the two other eigenvalues are complex conjugate pairs: $\xi_{1,2} = \xi_r \pm i\xi_i$, and ξ_3 is real, where ξ_r and ξ_i are real numbers.

The cases $\Delta < 0$ and $\Delta > 0$ correspond to the non-focal and focal regions, respectively. The surface $\Delta = 0$ can be split into two surfaces $r^{(1a)}$ and $r^{(1b)}$, which are given as

$$P(9Q - 2P^2) - 2(-3Q + P^2)^{3/2} - 27R = 0, \tag{5.6}$$

and

$$P(9Q - 2P^2) + 2(-3Q + P^2)^{3/2} - 27R = 0. \tag{5.7}$$

The two surfaces $r^{(1a)}$ and $r^{(1b)}$ osculate each other to form a cusp. In the region $\Delta > 0$, there is another surface $r^{(2)}$ which contains the points associated with purely imaginary eigenvalues

$$PQ - R = 0. \tag{5.8}$$

The P–Q–R space can thus be partitioned into different spatial regions by the surfaces $r^{(1a)}$, $r^{(1b)}$, $r^{(2)}$ and $R = 0$. The flow topology can be studied conveniently in the Q–R plane with a given value of P. The surfaces $r^{(1a)}$, $r^{(1b)}$, $r^{(2)}$ and $R = 0$ appear simply as curves on the Q–R plane, dividing the plane into different regions, which correspond to different topologies. The topological classifications in three representative Q–R planes are given in figure 16, while the description of acronyms for various flow topologies is listed in table 13 (Suman & Girimaji 2010). The term 'stable' means that the solution trajectories or the local streamlines of A_{ij} are directed toward the critical point, while the term 'unstable' suggests that the solution trajectories or the local streamlines of A_{ij} are pointed away from the critical point. Consequently, the stable topologies are associated with the tendency of a fluid element to be compressive, and the unstable topologies relate to the tendency of a fluid element to be expansive. Furthermore, when $\Delta > 0$, the fluid element exhibits a structure with rotational characteristics and an out-of-plane strain. When $\Delta < 0$, the fluid element appears to be non-swirling and straining. Besides, the fluid element exhibits a

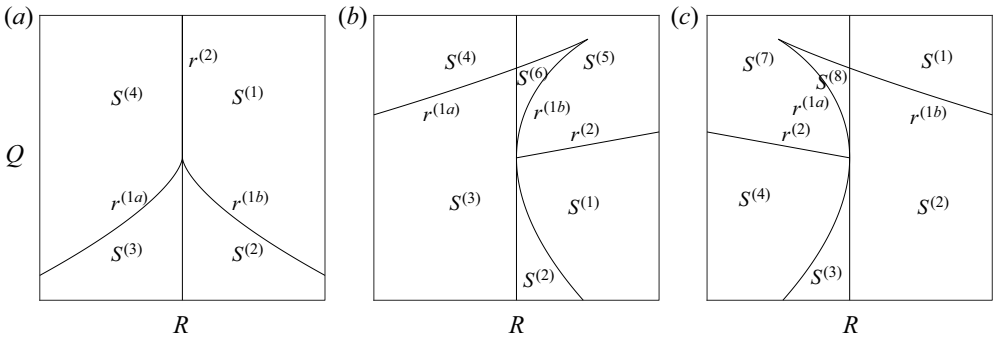

Figure 16. Topological classifications in three representative Q–R planes: (*a*) $P = 0$; (*b*) $P > 0$; (*c*) $P < 0$. The description of acronyms for various flow topologies is given in table 13.

Sector	Acronym	Description	Eigenvalues
$S^{(1)}$	UFC	Unstable focus/compressing	$\xi_r > 0$ and $\xi_3 < 0$
$S^{(2)}$	UN/S/S	Unstable node/saddle/saddle	$\xi_1 < 0$, $\xi_2 > 0$, and $\xi_3 > 0$
$S^{(3)}$	SN/S/S	Stable node/saddle/saddle	$\xi_1 < 0$, $\xi_2 < 0$, and $\xi_3 > 0$
$S^{(4)}$	SFS	Stable focus/stretching	$\xi_r < 0$ and $\xi_3 > 0$
$S^{(5)}$	SFC	Stable focus/compressing	$\xi_r < 0$ and $\xi_3 < 0$
$S^{(6)}$	SN/SN/SN	Stable node/stable node/stable node	$\xi_1 < 0$, $\xi_2 < 0$, and $\xi_3 < 0$
$S^{(7)}$	UFS	Unstable focus/stretching	$\xi_r > 0$ and $\xi_3 > 0$
$S^{(8)}$	UN/UN/UN	Unstable node/unstable node/unstable node	$\xi_1 > 0$, $\xi_2 > 0$, and $\xi_3 > 0$

Table 13. Description of acronyms of various flow topologies.

structure with two stretching directions and one contracting direction with positive R, and a structure with two contracting directions and one stretching direction with negative R.

The joint PDF of the normalized second and third invariants ($R/\langle Q_w\rangle^{3/2}$, $Q/\langle Q_w\rangle$, where $Q_w = \langle\omega^2\rangle/4$) at different dilatational levels for cases I_3 and I_5, as well as cases II_3 and II_5 are displayed in figures 17 and 18, respectively. In weak compression and weak expansion regions ($-0.05 < \theta/\theta' < 0.05$), the teardrop shape of the joint PDF is almost identical to that in weakly compressible turbulence (figures 17(*a*,*d*) and 18(*a*,*d*)). However, in the strong compression ($-2.55 < \theta/\theta' < -2.45$) and strong expansion ($2.45 < \theta/\theta' < 2.55$) regions, the relaxation effect on the volume fraction of the flow topology is significant, especially for the $M_t \approx 0.22$ cases. Tables 14 and 15 list the volume fractions of various flow topologies for the $M_t \approx 0.22$ and 0.68 cases, respectively. For case I_3, where the relaxation effect is significant, the shape of the joint PDF becomes rather sharp, with an extended tail around the right branch of the null-discriminant curve ($r^{(1b)}$) in the strong compression and strong expansion regions (figure 17*b*,*c*). The topologies $S^{(1)}$, $S^{(2)}$ and $S^{(4)}$ are thus predominant. As shown in table 14, for case I_3, the topologies $S^{(1)}$, $S^{(2)}$ and $S^{(4)}$ respectively account for volume fractions of 20.16 %, 31.41 % and 31.55 % in the strong compression region, and 15.86 %, 44.52 % and 30.95 % in the strong expansion region. For case I_5, where the flow compressibility is significantly enhanced, the tails around the right branch of the null-discriminant curve in the strong compression and strong expansion regions are shortened, and the angle between the curve $r^{(2)}$ and Q-axis enlarges. The strong compression region is therefore dominated by the stable topologies $S^{(3)}$, $S^{(4)}$ and $S^{(5)}$ with

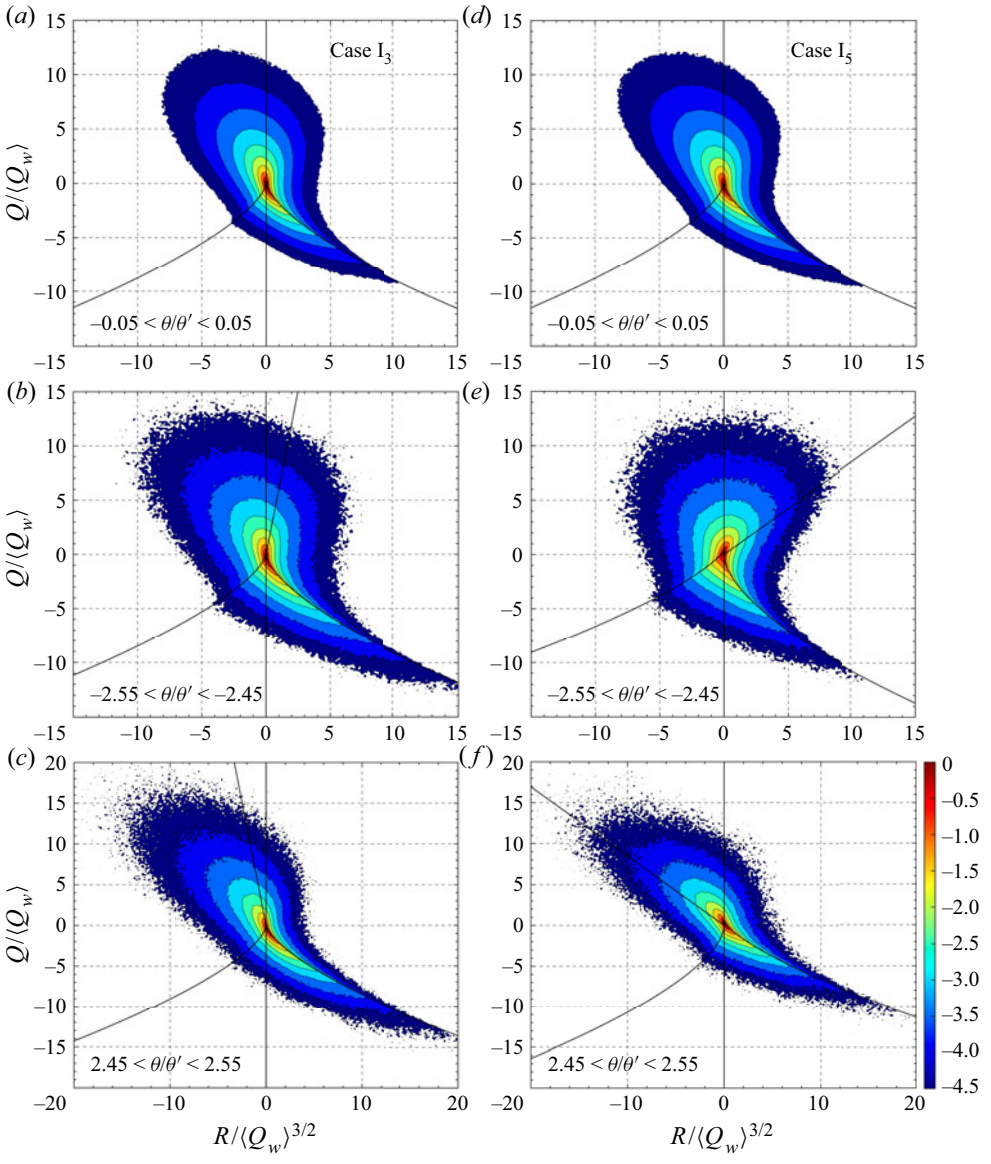

Figure 17. Logarithm of the joint PDF of the normalized second and third invariants of the velocity gradient tensor: (*a*,*d*) $-0.05 < \theta/\theta' < 0.05$; (*c*,*e*) $-2.55 < \theta/\theta' < -2.45$; (*c*,*e*) $2.45 < \theta/\theta' < 2.55$. (*a*–*c*) Case I_3, (*d*–*f*) case I_5.

volume fractions of 33.96%, 20.70% and 22.52%, respectively; while the strong expansion region is respectively dominated by the unstable topologies $S^{(1)}$, $S^{(2)}$ and $S^{(7)}$ with volume fractions of 13.62 %, 39.03 % and 36.39 %. Meanwhile, the volume fractions of topologies $S^{(6)}$ and $S^{(8)}$ are thus slightly enhanced with 1.95 % and 2.55 %, respectively.

For the $M_t \approx 0.68$ cases, the vibrational relaxation has little impact on the flow compressibility, and the relaxation effects on the volume fractions of the flow topologies are thus relatively weak, as shown in figure 18. In table 15, in comparison with the $M_t \approx 0.22$ cases in table 14, one can observe similar but smaller variations of the volume fractions of the flow topologies as the relaxation effect fades. For case II_3, the strong

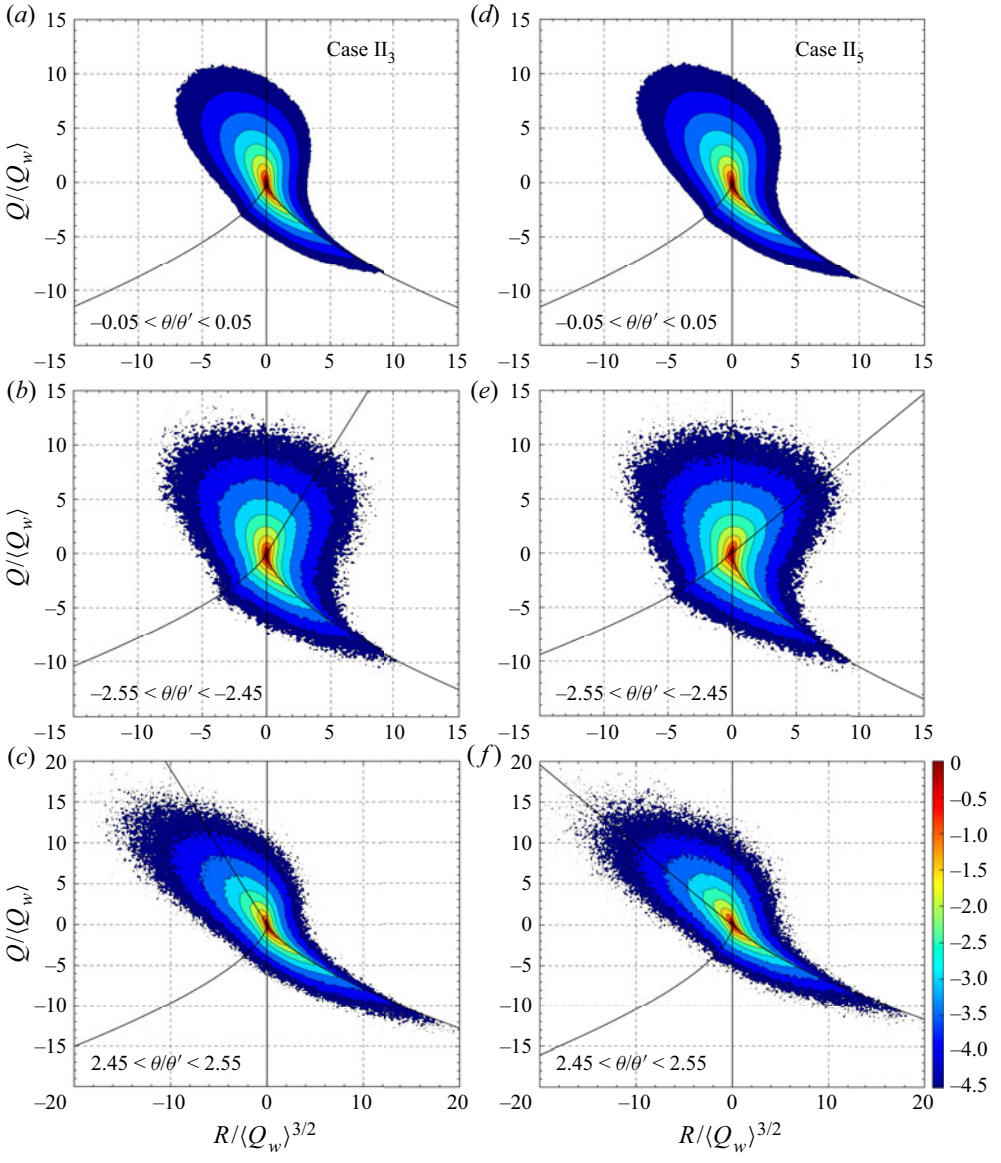

Figure 18. Logarithm of the joint PDF of the normalized second and third invariants of the velocity gradient tensor: (*a*,*d*) $-0.05 < \theta/\theta' < 0.05$; (*b*,*e*) $-2.55 < \theta/\theta' < -2.45$; (*c*,*f*) $2.45 < \theta/\theta' < 2.55$. (*a–c*) Case II_3, (*d–f*) case II_5.

compression region is dominated by the topologies $S^{(1)}$, $S^{(3)}$ and $S^{(4)}$ with volume fractions of 19.52%, 20.50% and 29.13%, respectively; while the strong expansion region is dominated by the topologies $S^{(2)}$ and $S^{(4)}$ with 36.76 % and 23.13 %, respectively. As the relaxation effect fades, for case II_5, the strong compression region is dominated by the stable topologies $S^{(3)}$, $S^{(4)}$ and $S^{(5)}$ with volume fractions of 30.69%, 23.30% and 19.15%, respectively; while the strong expansion region is respectively dominated by the unstable topologies $S^{(1)}$, $S^{(2)}$ and $S^{(7)}$ with 16.88 %, 34.74 % and 37.12 %.

Case	$S^{(1)}_{-2.5}$	$S^{(2)}_{-2.5}$	$S^{(3)}_{-2.5}$	$S^{(4)}_{-2.5}$	$S^{(5)}_{-2.5}$	$S^{(6)}_{-2.5}$	$S^{(1)}_{2.5}$	$S^{(2)}_{2.5}$	$S^{(3)}_{2.5}$	$S^{(4)}_{2.5}$	$S^{(7)}_{2.5}$	$S^{(8)}_{2.5}$
I_1	19.44	25.22	15.42	31.89	8.02	0.01	18.21	40.44	4.40	29.14	7.81	0.01
I_2	20.00	29.89	12.99	32.18	4.95	0.00	15.43	46.44	5.01	29.38	3.73	0.00
I_3	20.16	31.41	12.54	31.55	4.34	0.00	15.86	44.52	5.10	30.95	3.57	0.00
I_4	16.06	19.47	20.70	29.87	13.78	0.13	18.97	37.96	2.76	21.97	18.19	0.14
I_5	10.60	10.27	33.96	20.70	22.52	1.95	13.62	39.03	0.85	7.55	36.39	2.55
I_6	17.57	22.39	18.22	31.04	10.72	0.05	18.89	38.82	3.72	26.21	12.32	0.04
I_7	15.40	18.28	22.63	28.68	14.80	0.20	18.54	38.30	2.58	20.71	19.67	0.20

Table 14. Volume fractions of various flow topologies (%). Here, $S^{(i)}_{-2.5}$ and $S^{(i)}_{2.5}$ denote the topology $S^{(i)}$ in the $-2.55 < \theta/\theta' < -2.45$ and $2.45 < \theta/\theta' < 2.55$ regimes, respectively; $M_t \approx 0.22$.

Case	$S^{(1)}_{-2.5}$	$S^{(2)}_{-2.5}$	$S^{(3)}_{-2.5}$	$S^{(4)}_{-2.5}$	$S^{(5)}_{-2.5}$	$S^{(6)}_{-2.5}$	$S^{(1)}_{2.5}$	$S^{(2)}_{2.5}$	$S^{(3)}_{2.5}$	$S^{(4)}_{2.5}$	$S^{(7)}_{2.5}$	$S^{(8)}_{2.5}$
II_1	16.55	14.00	25.41	26.62	17.03	0.39	18.00	36.55	1.47	15.63	27.80	0.54
II_2	18.57	15.50	22.91	27.56	15.24	0.22	18.41	36.45	1.99	20.13	22.75	0.26
II_3	19.52	16.34	20.50	29.13	14.40	0.11	18.47	36.76	2.42	23.13	19.09	0.13
II_4	17.12	13.68	25.27	26.48	17.06	0.38	18.78	34.54	1.42	14.97	29.76	0.52
II_5	14.01	11.80	30.69	23.30	19.15	1.05	16.88	34.74	0.88	8.80	37.12	1.58
II_6	16.89	14.26	24.94	26.81	16.76	0.35	18.61	35.42	1.57	16.22	27.74	0.45
II_7	15.38	12.76	28.33	24.57	18.26	0.69	17.98	34.77	1.13	11.66	33.49	0.97

Table 15. Volume fractions of various flow topologies (%). Here, $S^{(i)}_{-2.5}$ and $S^{(i)}_{2.5}$ denote the topology $S^{(i)}$ in the $-2.55 < \theta/\theta' < -2.45$ and $2.45 < \theta/\theta' < 2.55$ regimes, respectively; $M_t \approx 0.68$.

Tables 16 and 17 list the relative contributions from various flow topologies to the local enstrophy production ($\omega_i\omega_j S^*_{ij}$) (%) for the $M_t \approx 0.22$ and 0.68 cases, respectively. When the relaxation effect is significant (e.g. cases I_3 and II_3), in both strong compression and strong expansion regions, the sum of relative contributions from topologies $S^{(2)}$ and $S^{(4)}$ is larger than 90 %, indicating that they make major contributions to the locally averaged enstrophy production. As the relaxation effect fades, in the strong compression region, the relative contributions from topologies $S^{(2)}$ and $S^{(4)}$ decrease, while those from topologies $S^{(3)}$ and $S^{(5)}$ increase. For instance, from case I_3 to case I_5, the relative contributions from topologies $S^{(2)}$ and $S^{(4)}$ decrease respectively from 27.71 % and 71.11 % to 11.61 % and 59.29 %; while those of topologies $S^{(3)}$ and $S^{(5)}$ increase respectively from 6.00 % and 0.49 % to 14.06 % and 12.29 %. In the strong expansion region, the relative contributions from topologies $S^{(2)}$, $S^{(4)}$ and $S^{(7)}$ increase as the relaxation effect fades. Meanwhile, the significance of topology $S^{(1)}$ is amplified, and it plays a destruction role for enstrophy. For example, the relative contribution from topology $S^{(1)}$ reduces from 3.21 % (case I_3) to -37.15 % (case I_5), and from 0.82 % (case II_3) to -22.66 % (case II_5) (tables 16 and 17).

6. Discussion

The studies of the statistical properties of compressible isotropic turbulence in vibrational non-equilibrium were pioneered by Donzis & Maqui (2016), and followed by Khurshid & Donzis (2019) and Zheng *et al.* (2020). Different from our previous investigation (Zheng *et al.* 2020), in the companion paper (Zheng *et al.* 2021) and the present work, we mainly focus on the statistical properties of compressible isotropic turbulence in vibrational non-equilibrium with a large-scale thermal forcing. Although the large-scale

Case	$S^{(1)}_{-2.5}$	$S^{(2)}_{-2.5}$	$S^{(3)}_{-2.5}$	$S^{(4)}_{-2.5}$	$S^{(5)}_{-2.5}$	$S^{(6)}_{-2.5}$	$S^{(1)}_{2.5}$	$S^{(2)}_{2.5}$	$S^{(3)}_{2.5}$	$S^{(4)}_{2.5}$	$S^{(7)}_{2.5}$	$S^{(8)}_{2.5}$
I_1	−4.14	23.35	6.54	73.00	1.24	0.00	0.37	27.21	3.00	68.61	0.80	0.00
I_2	−5.17	27.30	6.03	71.25	0.59	0.00	3.97	28.59	3.42	63.66	0.36	0.00
I_3	−5.30	27.71	6.00	71.11	0.49	0.00	3.21	26.60	3.38	66.44	0.37	0.00
I_4	−0.91	18.08	8.10	71.16	3.57	0.00	−8.88	28.92	2.35	74.19	3.41	0.00
I_5	2.55	11.61	14.06	59.29	12.29	0.21	−37.15	43.70	1.49	82.15	10.14	−0.33
I_6	−2.56	20.95	7.26	72.24	2.10	0.00	−2.73	27.95	2.82	70.43	1.53	0.00
I_7	−0.66	17.58	8.62	70.34	4.12	0.01	−9.55	29.00	2.32	74.60	3.64	0.00

Table 16. Relative contributions from various flow topologies to the locally averaged enstrophy production ($\omega_i\omega_j S^*_{ij}$) (%). Here, $S^{(i)}_{-2.5}$ and $S^{(i)}_{2.5}$ denote the topology $S^{(i)}$ in the $-2.55 < \theta/\theta' < -2.45$ and $2.45 < \theta/\theta' < 2.55$ regimes, respectively; $M_t \approx 0.22$.

Case	$S^{(1)}_{-2.5}$	$S^{(2)}_{-2.5}$	$S^{(3)}_{-2.5}$	$S^{(4)}_{-2.5}$	$S^{(5)}_{-2.5}$	$S^{(6)}_{-2.5}$	$S^{(1)}_{2.5}$	$S^{(2)}_{2.5}$	$S^{(3)}_{2.5}$	$S^{(4)}_{2.5}$	$S^{(7)}_{2.5}$	$S^{(8)}_{2.5}$
II_1	−2.07	14.48	9.86	71.36	6.34	0.03	−2.46	25.72	1.84	67.72	7.19	0.00
II_2	−5.31	16.20	8.78	75.44	4.86	0.01	0.31	23.84	2.06	68.95	4.84	0.00
II_3	−7.18	16.64	8.10	78.41	4.04	0.00	0.82	24.22	2.17	69.39	3.39	0.00
II_4	−2.75	13.68	9.65	72.90	6.49	0.03	−6.04	25.06	1.77	71.06	8.16	0.00
II_5	0.74	12.30	12.24	65.41	9.21	0.11	−22.66	32.72	1.50	78.24	10.29	−0.10
II_6	−2.32	14.53	9.62	72.12	6.03	0.02	−4.24	25.13	1.80	70.12	7.20	0.00
II_7	−0.53	13.42	10.96	68.32	7.76	0.06	−10.72	27.51	1.66	71.68	9.89	−0.02

Table 17. Relative contributions from various flow topologies to the locally averaged enstrophy production ($\omega_i\omega_j S^*_{ij}$) (%). Here, $S^{(i)}_{-2.5}$ and $S^{(i)}_{2.5}$ denote the topology $S^{(i)}$ in the $-2.55 < \theta/\theta' < -2.45$ and $2.45 < \theta/\theta' < 2.55$ regimes, respectively; $M_t \approx 0.68$.

thermal forcing adopted in the present simulations cannot completely reproduce the shock-induced heating in high-speed flows, it provides a simplified way to investigate the effects of large-scale thermal forcing on the small-scale statistical properties of turbulence. In the present simulations, the vibrational relaxation effect acts as a buffer between the translational–rotational temperature and the vibrational temperature, relieving the temperature fluctuations; while the thermal forcing injects the temperature fluctuations at large scales. There is an inverse effect between the vibrational relaxation and the large-scale thermal forcing, and they determine the flow compressibility together with the turbulent Mach number (as shown in figures 1 and 2). The vibrational relaxation weakens the flow compressibility and the large-scale thermal forcing enhances it. Furthermore, because the dimensionless relaxation time is determined by the local temperature and pressure (2.9), and the departure between the translational–rotational and vibrational temperatures is dependent of the turbulent fluctuation, the state of vibrational non-equilibrium thus closely relates to the flow compressibility for a flow system with given M_t and large-scale thermal forcing. Here, the thermal forcing has a weaker impact on the flow compressibility for the $M_t \approx 0.68$ cases. This should be attributed to the fact that their own temperature fluctuations at large scales are comparable to the thermal forcing in these cases.

In Zheng *et al.* (2021), we found that the turbulent Mach number and vibrational relaxation have little influence on the fluctuations of solenoidal velocity and pressure components, and have a significant effect on the fluctuations of dilatational velocity and pressure components. Similarly, in the present investigation, the impacts of local

dilatation and vibrational relaxation on the conditional PDFs of normalized eigenvalues of D_{ij}^S and the alignments between the vorticity and eigenvectors of D_{ij}^S are negligible. The preferred ratio of eigenvalues of D_{ij}^S and the alignments between the vorticity and eigenvectors of D_{ij}^S are close to those of incompressible turbulence. On the contrary, the conditional PDFs of normalized eigenvalues of D_{ij}^D and the alignments between vorticity and eigenvectors of D_{ij}^D closely relate to the local dilatation and vibrational relaxation. Consequently, the ratio of $\langle \omega^2 \lambda_i^S \mathrm{Cos}^2(\omega, \Lambda_i^S)/\langle \omega_i \omega_j S_{ij}^* \rangle \rangle$ roughly remains constant despite varying the state of vibrational non-equilibrium (tables 9 and 11), while the ratio of $\langle \omega^2 \lambda_i^D \mathrm{Cos}^2(\omega, \Lambda_i^D)/\langle \omega_i \omega_j S_{ij}^* \rangle \rangle$ is sensitive to the state of vibrational non-equilibrium (tables 10 and 12). On the other hand, the volume fractions of various flow topologies closely relate to the flow compressibility, and are dependent of the state of vibrational non-equilibrium (tables 14 and 15), particularly for the $M_t \approx 0.22$ cases. However, as revealed in tables 16 and 17, the relative contributions from various flow topologies to the locally averaged enstrophy production are somewhat confusing due to the advent of vibrational relaxation. The slight change in volume fraction may lead to a significant difference in the relative contributions to the locally averaged enstrophy production (e.g. $S_{2.5}^{(1)}$ in the strong expansion region, tables 14–17). The mechanism behind this confusing phenomenon remains unclear, and requires further in-depth investigation.

7. Summary and conclusions

In this paper, the statistically steady compressible isotropic turbulence in vibrational non-equilibrium is numerically investigated. The large-scale momentum forcing is used to maintain the turbulence in a statistically stationary state, and the large-scale thermal forcing is adopted to inject temperature fluctuations. Two series of cases are employed with the turbulent Mach number (M_t) approximately equal to 0.22 and 0.68, and the Taylor Reynolds number (Re_λ) is approximately 157.5. The attention focuses on the combined effects of large-scale thermal forcing and vibrational relaxation on the enstrophy production and flow topology. The main conclusions are briefly summarized as follows.

The large-scale thermal forcing and vibrational relaxation have a great influence on the flow compressibility for the $M_t \approx 0.22$ cases. As the relaxation effect fades, the flow compressibility is strongly enhanced and the clear shocklet structures lie across the flow field. For the $M_t \approx 0.68$ cases, the large-scale thermal forcing has a relative weaker impact on the flow compressibility. The deviatoric strain-rate tensor can be decomposed into the dilatational and solenoidal components. For the $M_t \approx 0.22$ cases, due to the relaxation effect, the correlation between the dilatation and solenoidal component of the deviatoric strain-rate tensor is enhanced, while the correlation between the dilatation and dilatational component of the deviatoric strain-rate tensor is weakened. Furthermore, for the $M_t \approx 0.68$ cases, the relaxation effects on the correlation between the dilatation and the deviatoric strain components are negligible.

The net enstrophy production term ($\omega_i \omega_j S_{ij}^*$) is decomposed into the solenoidal ($\omega_i \omega_j D_{ij}^S$), dilatational ($\omega_i \omega_j D_{ij}^D$) and isotropic dilatational ($-(1/6)\theta\omega^2$) terms. From the full flow field perspective, the net enstrophy production mainly stems from the solenoidal term. For the dilatational and isotropic dilatational terms, although their local magnitudes can be considerable, the positive values in the compression region and the negative values in the expansion region cancel out on average. Furthermore, the variations of the net

enstrophy production term and its components depend closely on the local dilatation and vibration relaxation.

The eigenframe of strain-rate tensor is helpful to investigate the mechanism of enstrophy production. Effects of the local dilatation and vibrational relaxation on the conditional PDFs of normalized eigenvalues of D_{ij}^S are negligible. In the overall flow field, the preferred ratio of eigenvalues of D_{ij}^S and the alignments between vorticity and eigenvectors of D_{ij}^S are similar to those of incompressible and weakly compressible turbulent flows. On the other hand, the conditional PDFs of the normalized eigenvalues of D_{ij}^D, and the alignments between the vorticity and eigenvectors of D_{ij}^D, are closely related to the vibrational relaxation and local dilatation. The first normalized eigenvalue with $\beta_1^D \approx -0.81$ dominates in the compression region, and the third normalized eigenvalue with $\beta_3^D \approx 0.80$ in the expansion region. The intermediate eigenvalue β_2^D tends to be positive in the compression region, and negative in the expansion region. When the flow compressibility is weak, there is a tendency for the vorticity to be perpendicular to the first eigenvector and align with the third eigenvector in the compressible region, while strongly aligning with the first eigenvector and being perpendicular to the third eigenvector in the expansion region. The stronger the flow compressibility, the less significant the alignments between the vorticity and eigenvectors of D_{ij}^D. The solenoidal and dilatational terms of net enstrophy production can be rewritten as $\omega^2\lambda_i^S\cos^2(\omega, \Lambda_i^S)/\langle\omega_i\omega_j S_{ij}^*\rangle$ and $\omega^2\lambda_i^D\cos^2(\omega, \Lambda_i^D)/\langle\omega_i\omega_j S_{ij}^*\rangle$, respectively. Dependencies of $\omega^2\lambda_i^S\cos^2(\omega, \Lambda_i^S)/\langle\omega_i\omega_j S_{ij}^*\rangle$ on the local dilatation are mainly affected by the vorticity, while those of $\omega^2\lambda_i^D\cos^2(\omega, \Lambda_i^D)/\langle\omega_i\omega_j S_{ij}^*\rangle$ are affected by the vorticity, eigenvalues and alignments between vorticity and strain eigenvectors.

The topological classification proposed by Chong *et al.* (1990) is employed to decompose the flow field into various flow topologies. From the joint PDF of the normalized second and third invariants of the velocity gradient tensor conditioned on the local dilatation, the classical teardrop shape in incompressible or weakly compressible turbulent flows still holds in the weak compression and weak expansion regions. In the strong compression and strong expansion regions, the relaxation effects on the volume fractions of the flow topologies are significant for the $M_t \approx 0.22$ cases. When the relaxation effect is significant, the joint PDF has an extended tail around the right branch of the null-discriminant curve in the strong compression and strong expansion regions; and thus the topologies UFC, UN/S/S and SFS are predominant. As the relaxation effect fades, the tails around the right branch of the null-discriminant curve in the strong compression and strong expansion regions are shortened. The strong compression region is dominated by the stable topologies SN/S/S, SFS and SFC, while the strong expansion region is dominated by the unstable topologies UFC, UN/S/S and UFS. For the $M_t \approx 0.68$ cases, the relaxation effects on the volume fractions of flow topologies are relatively weak. In comparison with the $M_t \approx 0.22$ cases, similar but smaller variations of the volume fractions of the flow topologies are observed as the relaxation effect fades.

The relaxation effects on the relative contributions from various flow topologies to the local enstrophy production are similar for both $M_t \approx 0.22$ and 0.68 cases. In the strong compression and strong expansion regions, as the relaxation effect is significant, the topologies UN/S/S and SFS make major contributions to the local enstrophy production with the sum of their relative contributions being larger than 90 %. As the relaxation effect fades, in the strong compression region, the relative contributions from topologies UN/S/S and SFS decrease, while those from topologies SN/S/S and SFC increase; on the other

hand, in the strong expansion region, the relative contributions from topologies UN/S/S, SFS and UFS increase, while the significance of topology UFC is strongly amplified for enstrophy destruction.

Funding. This work is supported by the National Natural Science Foundation of China (Grant Nos. 12172161, 12161141017, 92052301, 91752201, 91952104 and 11902139), NSFC Basic Science Center Program for Multiscale Problems in Nonlinear Mechanics (Grant No. 11988102), China Postdoctoral Science Foundation (Grant No.2019M652703), Technology and Innovation Commission of Shenzhen Municipality (Grant Nos. KQTD20180411143441009 and JCYJ20170412151759222), Key Special Project for Introduced Talents Team of Southern Marine Science and Engineering Guangdong Laboratory (Guangzhou) (Grant No. GML2019ZD0103) and by Department of Science and Technology of Guangdong Province (Grant No. 2019B21203001). This work is also supported by Center for Computational Science and Engineering of Southern University of Science and Technology.

Declaration of interests. The authors report no conflict of interest.

Author ORCIDs.
Qinmin Zheng https://orcid.org/0000-0002-0188-4835;
Jianchun Wang https://orcid.org/0000-0001-5101-7791.

References

Anderson, J.D. Jr. 2006 *Hypersonic and High-Temperature Gas Dynamics*. American Institute of Aeronautics and Astronautics.

Ashurst, W.T., Kerstein, A.R., Kerr, R.M. & Gibson, C.H. 1987 Alignment of vorticity and scalar gradient with strain rate in simulated Navier–Stokes turbulence. *Phys. Fluids* **30** (8), 2343–2353.

Balsara, D.S. & Shu, C.-W. 2000 Monotonicity preserving weighted essentially non-oscillatory schemes with increasingly high order of accuracy. *J. Comput. Phys.* **160** (2), 405–452.

Bijlard, M.J., Oliemans, R.V.A., Portela, L.M. & Ooms, G. 2010 Direct numerical simulation analysis of local flow topology in a particle-laden turbulent channel flow. *J. Fluid Mech.* **653**, 35–56.

Blackburn, H.M., Mansour, N.N. & Cantwell, B.J. 1996 Topology of fine-scale motions in turbulent channel flow. *J. Fluid Mech.* **310**, 269–292.

Buaria, D., Bodenschatz, E. & Pumir, A. 2020 Vortex stretching and enstrophy production in high Reynolds number turbulence. *Phys. Rev. Fluids* **5** (10), 104602.

Candler, G.V. 2019 Rate effects in hypersonic flows. *Annu. Rev. Fluid Mech.* **51** (1), 379–402.

Carter, D.W. & Coletti, F. 2018 Small-scale structure and energy transfer in homogeneous turbulence. *J. Fluid Mech.* **854**, 505–543.

Chong, M.S., Perry, A.E. & Cantwell, B.J. 1990 A general classification of three-dimensional flow fields. *Phys. Fluids* A **2** (5), 765–777.

Chong, M.S., Soria, J., Perry, A.E., Chacin, J., Cantwell, B.J. & Na, Y. 1998 Turbulence structures of wall-bounded shear flows found using DNS data. *J. Fluid Mech.* **357**, 225–247.

Danish, M., Sinha, S.S. & Srinivasan, B. 2016 Influence of compressibility on the lagrangian statistics of vorticity–strain-rate interactions. *Phys. Rev.* E **94** (1), 013101.

Donzis, D. & Jagannathan, S. 2013 Fluctuations of thermodynamic variables in stationary compressible turbulence. *J. Fluid Mech.* **733**, 221–244.

Donzis, D.A. & Maqui, A.F. 2016 Statistically steady states of forced isotropic turbulence in thermal equilibrium and non-equilibrium. *J. Fluid Mech.* **797**, 181–200.

Erlebacher, G. & Sarkar, S. 1993 Statistical analysis of the rate of strain tensor in compressible homogeneous turbulence. *Phys. Fluids* A **5** (12), 3240–3254.

Fiévet, R. & Raman, V. 2018 Effect of vibrational nonequilibrium on isolator shock structure. *J. Propul. Power* **34** (5), 1334–1344.

Gottlieb, S. & Shu, C.-W. 1998 Total variation diminishing Runge–Kutta schemes. *Math. Comput.* **67** (221), 73–85.

Hamlington, P.E., Schumacher, J. & Dahm, W.J.A. 2008 Local and nonlocal strain rate fields and vorticity alignment in turbulent flows. *Phys. Rev.* E **77** (2), 026303.

Khurshid, S. & Donzis, D.A. 2019 Decaying compressible turbulence with thermal non-equilibrium. *Phys. Fluids* **31** (1), 015103.

Knisely, C.P. & Zhong, X. 2020 Impact of vibrational nonequilibrium on the supersonic mode in hypersonic boundary layers. *AIAA J.* **58** (4), 1704–1714.

LEE, K., GIRIMAJI, S.S. & KERIMO, J. 2009 Effect of compressibility on turbulent velocity gradients and small-scale structure. *J. Turbul.* **10**, N9.

LELE, S.K. 1992 Compact finite difference schemes with spectral-like resolution. *J. Comput. Phys.* **103** (1), 16–42.

LÜTHI, B., TSINOBER, A. & KINZELBACH, W. 2005 Lagrangian measurement of vorticity dynamics in turbulent flow. *J. Fluid Mech.* **528**, 87–118.

MENEVEAU, C. 2011 Lagrangian dynamics and models of the velocity gradient tensor in turbulent flows. *Annu. Rev. Fluid Mech.* **43**, 219–245.

NOMURA, K.K. & DIAMESSIS, P.J. 2000 The interaction of vorticity and rate-of-strain in homogeneous sheared turbulence. *Phys. Fluids* **12** (4), 846–864.

NOMURA, K.K. & POST, G.K. 1998 The structure and dynamics of vorticity and rate of strain in incompressible homogeneous turbulence. *J. Fluid Mech.* **377**, 65–97.

OOI, A., MARTIN, J., SORIA, J. & CHONG, M.S. 1999 A study of the evolution and characteristics of the invariants of the velocity-gradient tensor in isotropic turbulence. *J. Fluid Mech.* **381**, 141–174.

PAPAPOSTOLOU, V., WACKS, D.H., CHAKRABORTY, N., KLEIN, M. & IM, H.G. 2017 Enstrophy transport conditional on local flow topologies in different regimes of premixed turbulent combustion. *Sci. Rep.* **7** (1), 11545.

PARASHAR, N., SINHA, S.S. & SRINIVASAN, B. 2019 Lagrangian investigations of velocity gradients in compressible turbulence: lifetime of flow-field topologies. *J. Fluid Mech.* **872**, 492–514.

PETERSEN, M.R. & LIVESCU, D. 2010 Forcing for statistically stationary compressible isotropic turbulence. *Phys. Fluids* **22** (11), 116101.

PIROZZOLI, S. & GRASSO, F. 2004 Direct numerical simulations of isotropic compressible turbulence: influence of compressibility on dynamics and structures. *Phys. Fluids* **16** (12), 4386–4407.

SAMTANEY, R., PULLIN, D.I. & KOSOVIĆ, B. 2001 Direct numerical simulation of decaying compressible turbulence and shocklet statistics. *Phys. Fluids* **13** (5), 1415–1430.

DA SILVA, C.B. & PEREIRA, J.C.F. 2008 Invariants of the velocity-gradient, rate-of-strain, and rate-of-rotation tensors across the turbulent/nonturbulent interface in jets. *Phys. Fluids* **20** (5), 055101.

SUMAN, S. & GIRIMAJI, S.S. 2010 Velocity gradient invariants and local flow-field topology in compressible turbulence. *J. Turbul.* **11**, N2.

TSINOBER, A., KIT, E. & DRACOS, T. 1992 Experimental investigation of the field of velocity gradients in turbulent flows. *J. Fluid Mech.* **242**, 169–192.

VAGHEFI, N.S. & MADNIA, C.K. 2015 Local flow topology and velocity gradient invariants in compressible turbulent mixing layer. *J. Fluid Mech.* **774**, 67–94.

VINCENTI, W.G. & KRUGER, C.H. 1965 *Introduction to Physical Gas Dynamics*. Wiley.

WALLACE, J.M. 2009 Twenty years of experimental and direct numerical simulation access to the velocity gradient tensor: what have we learned about turbulence? *Phys. Fluids* **21** (2), 021301.

WANG, J., SHI, Y., WANG, L.-P., XIAO, Z., HE, X. & CHEN, S. 2011 Effect of shocklets on the velocity gradients in highly compressible isotropic turbulence. *Phys. Fluids* **23** (12), 125103.

WANG, J., SHI, Y., WANG, L.-P., XIAO, Z., HE, X.T. & CHEN, S. 2012 Effect of compressibility on the small-scale structures in isotropic turbulence. *J. Fluid Mech.* **713**, 588–631.

WANG, J., WAN, M., CHEN, S., XIE, C., WANG, L.-P. & CHEN, S. 2019 Cascades of temperature and entropy fluctuations in compressible turbulence. *J. Fluid Mech.* **867**, 195–215.

WANG, J., WAN, M., CHEN, S., XIE, C., ZHENG, Q., WANG, L.-P. & CHEN, S. 2020 Effect of flow topology on the kinetic energy flux in compressible isotropic turbulence. *J. Fluid Mech.* **883**, A11.

WANG, J., WANG, L.-P., XIAO, Z., SHI, Y. & CHEN, S. 2010 A hybrid numerical simulation of isotropic compressible turbulence. *J. Comput. Phys.* **229** (13), 5257–5279.

WANG, L. & LU, X.-Y. 2012 Flow topology in compressible turbulent boundary layer. *J. Fluid Mech.* **703**, 255–278.

ZHENG, Q., WANG, J., ALAM, M.M., NOACK, B.R., LI, H., WAN, M. & CHEN, S. 2021 Transfer of internal energy fluctuation in compressible isotropic turbulence with vibrational nonequilibrium. *J. Fluid Mech.* **883**, A26.

ZHENG, Q., WANG, J., NOACK, B.R., LI, H., WAN, M. & CHEN, S. 2020 Vibrational relaxation in compressible isotropic turbulence with thermal nonequilibrium. *Phys. Rev. Fluids* **5**, 044602.

ZHOU, Y., NAGATA, K., SAKAI, Y., ITO, Y. & HAYASE, T. 2016 Enstrophy production and dissipation in developing grid-generated turbulence. *Phys. Fluids* **28** (2), 025113.